공학박사 학위논문

# Metal–Insulator Transition in $Fe_3O_4$ Nanocrystals

## 산화철 나노입자의 금속-절연체 전이 현상

**2019년 2월**

서울대학교 대학원

화학생물공학부

이 지 수

# Metal–Insulator Transition in $Fe_3O_4$ Nanocrystals
# 산화철 나노입자의 금속-절연체 전이 현상

지도교수 현 택 환

이 논문을 공학박사 학위논문으로 제출함

2018 년 12 월

서울대학교 대학원
화학생물공학부
이 지 수

이지수의 박사 학위논문을 인준함

2018 년 12 월

위 원 장 _____ (인)

부위원장 _____ (인)

위 원 _____ (인)

위 원 _____ (인)

위 원 _____ (인)

# Abstract

## Metal–Insulator Transition in $Fe_3O_4$ Nanocrystals

Jisoo Lee

Chemical and Biological Engineering

The Graduate School

Seoul National University

Nanocrystals are particles that are at least 100 nm wide in one direction. Nanocrystals, unlike their bulk counterparts, contain very few atoms that make up a single particle, leading to very different physical and chemical properties. In order to utilize the desired nanocrystals, nanocrystals must be able to be synthesized in a uniform and desired shape.

In the first chapter of this thesis, I will discuss how nanocrystals can be synthesized in a uniform and desired shape. These synthesized nanocrystals allow us to study their unusual properties. In

the second chapter, I studied size-dependent metal-insulator transition phenomena on uniform-sized iron oxide (magnetite) nanocrystals with various sizes. The smaller the nanocrystals, the greater the change in metal-insulator transition phenomena. In the third chapter, I synthesized core/shell $Fe_3O_4$/ferrite nanocrystals and investigated their metal-insulator transition phenomena. As the types and thickness of the shell materials are varied, changes in the metal-insulator transition phenomena were observed.

**Keywords:** nanocrystals, nanoparticles, iron oxide, magnetite, metal-insulator transition, the Verwey transition

**Student number: 2010-22819**

# Contents

# List of Tables

# List of Figures

# Chapter 1. Introduction:
# Nucleation and growth of inorganic nanoparticles

## 1.1 Introduction

In the past two decades, a tremendous interest in nanoscience and nanotechnology has promoted a rapid development in the synthesis and characterization of various kinds of nanomaterials [1-8]. The novel characteristics of these nanomaterials, and the resulting potential for applications, derive from the fact that their properties lie between those of molecules and crystalline solids. As the size of a particle increases from the angstrom to the nanometer and micrometer scale, several fundamental changes occur. The molecular symmetry changes to a crystal lattice with periodic long range order [9], discrete energy levels turn into a continuous band structure [10] and electrons confined in the molecular orbitals become delocalized [11]. Advanced synthetic methods have made it possible to manipulate these changes to develop nanomaterials with designed functionalities. For example, nowadays, routine protocols are available to prepare monodisperse single-

component nanoparticles, as well as multicomponent nanoparticles with various shapes and compositions. The impact of nanotechnology has propagated from fundamental nanoscience to many applications, including electronics [5, 12], photonics [13, 14], plasmonics [15, 16], energy conversion and storage [17-20], catalysis [21, 22] and biomedical engineering [23-25]. In turn, the performances of the nanomaterials required for these applications impose new challenges on nanoscience. In particular, there is a gap between the need for purposely designed nanoparticles and our current understanding of their formation mechanism. Until the early 2000s, size uniformity was the biggest issue in nanoparticle synthesis, because it is critical for the production of ensembles of nanoparticles with homogeneous physicochemical properties [1, 2, 4]. At the time, various synthetic protocols for the synthesis of monodisperse nanoparticles were developed by empirical approaches. Nowadays, the synthesis of multicomponent nanoparticles is rapidly gaining importance, motivated by the demand for enhanced performance and/or multifunctionality for various applications [26-29]. However, with increasing reaction complexity, conventional trial-and-error approaches become very inefficient; synthetic methods should instead be based on a clear

understanding of the formation mechanism of particles, which has yet to be achieved. Recently, the current state of nanochemistry was described as similar to that of organic chemistry in the early twentieth century, when it was transitioning from an empirical art to a science [30]. In a similar way, we believe that the development of nanochemistry will become increasingly dependent on fundamental understanding.

The characterization of nanomaterials constitutes both a challenge and an opportunity for chemistry and materials science. Characterization techniques optimized for molecules or solids are often not sufficient to fully characterize nanoparticles, thus a combination of multiple techniques is required [31]. On the other hand, studying the formation mechanisms of nanoparticles can provide unique opportunities to explore the 'forbidden' region of the molecule-to-solid transition, in which molecular chemistry meets solid state science. In this Review, we discuss recent advances in the study of the formation mechanisms at work during nanoparticle synthesis. In its early times, the theory of nucleation and growth of nanoparticles was largely borrowed from classical colloid chemistry [1, 32]. However, with the development of nanochemistry, many nonclassical behaviours were

identified, revealing new aspects of crystallization at the nanometer scale.

We summarize the formation mechanisms of nanoparticles by organizing them into four sections. First, stable nanoclusters representing the ‘missing link’ between molecules and solids are discussed. Second, various nonclassical nucleation models in which the nucleation kinetics is altered by the presence of intermediate species are presented, followed by the growth of nanoparticles via the assembly and merging of primary particles. Last, heterogeneous nucleation models for multicomponent nanoparticles are presented.

## 1.2 Molecule-to-solid transition

### 1.2.1 Structure of molecular clusters

In the classical crystallization theory, there is a clear boundary dividing a crystal from its monomeric building units. However, in nanoscale materials, it becomes evident that this boundary is not abrupt but rather a broad spectrum that spans intermediate structures between molecules and solids. The study of 'missing links' connecting these two categories aids our understanding of how a molecular structure evolves into a crystal [33-35].

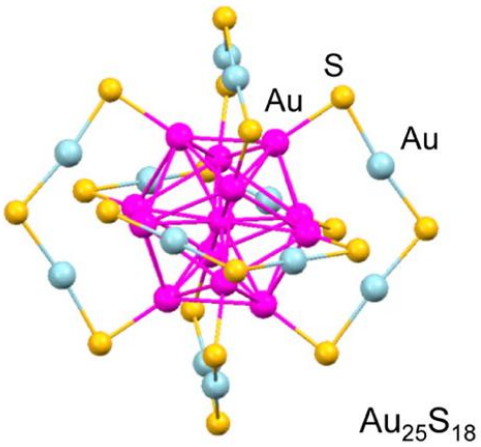


**Figure 1.1** Structures of cluster molecules and their size-dependent properties. Structure of an $Au_{25}RS_{18}$ cluster. Sulfur and gold atoms of staple motifs are in yellow and blue, respectively, and the $Au_{13}$ core is in purple. Panel is adapted with permission from Ref. [36], American Chemical Society.

The development of synthesis and characterization techniques for ligand-passivated metal clusters has allowed a generalization of the geometric closed-shell theory, leading to the concept of 'super atoms' [37], which are clusters that exhibit some of the properties of elemental atoms. For example, the structure of $[Au_{25}(RS)_{18}]^{-}$, where RS is a thiol ligand, can be described as an $Au_{13}$ core protected by six $Au_2(SR)_3$ 'staple' motifs [36, 38-43] (Figure 1.1). The $Au_{13}$ core corresponds to a closed-shell structure with K = 2, which gives the cluster good structural rigidity. In addition, this cluster molecule has a full-shell configuration of electronic energy levels, which is analogous to the electronic configuration of noble gas atoms. Indeed, excluding 18 thiolate gold ions, there are 7 gold atoms donating a valence electron from the $6s^1$ orbital, plus one electron from the negative charge of the cluster. These 8 electrons fill the molecular orbitals, so that the overall electron configuration resembles the valence shell of neon, $2s^2 2p^6$ [37]. The same principle applies to other structures. The structure of $Au_{102}$(p-MBA)$_{44}$ (p-MBA, p-mercaptobenzoic acid) was reported with atomic precision [43], and it was shown that, although the geometric structure of $Au_{102}$ clusters is not consistent with the closed-shell model, these clusters have good chemical stability because they satisfy the full

electron shell condition with 58 (102 Au − 44 thiolated Au) valence electrons [44]. Notably, not all clusters satisfy either geometric or electronic full-shell conditions, as shown in the case of $Au_{68}$ clusters, which suggests that other stabilization factors are at work [45].

## 1.3 Prenucleation and nucleation periods

### 1.3.1 Nucleation models

Nucleation is the beginning of condensation and is one of the most ubiquitous phenomena in the universe: stars and planets condense from the interstellar medium [46], clouds and rain drops condense from water vapour, and nanoparticles condense from supersaturated solutions. If the condensed phase is crystalline, nucleation is not only accompanied by an abrupt increase in local density, but it also causes an increase in local order. Therefore, the study of nucleation processes can shed light on the general tendency towards self-organization in nature [47].

In solution, there are three possible nucleation models: classical nucleation, spinodal decomposition and nonclassical nucleation (Figure 1.2) [48, 49]. In the classical nucleation theory, homogeneous nucleation has a high thermodynamic energy barrier that originates from the high surface-to-volume ratio of the nucleus. Given that the surface energy per area, $\gamma$, and the bulk energy per volume, $\Delta G_v$, are constant, the free energy change, $\Delta G$, resulting from homogeneous nucleation is written as

$$\Delta G_{hom}(r) = 4\pi r^2\gamma + 4/3\pi r^3\Delta G_{\mathrm{v}} \quad (1)$$

where r is the radius of a spherical nucleus [50]. From the condition $d[\Delta G_{\mathrm{hom}}(r)]/dr = 0$, the critical radius, $r^* = -2\gamma/\Delta G_{\mathrm{v}}$, is derived. Only the nuclei with $r \geq r^*$ can spontaneously grow into larger particles ($d[\Delta G_{\mathrm{hom}}(r)]/dr < 0$), whereas those with $r < r^*$ will dissolve in the solution. This energy barrier is important in the synthesis of uniformly sized nanoparticles because it suppresses the random formation of particles in the course of the reaction and induces short bursts of nucleation under high supersaturation [51, 52]. By contrast, spinodal decomposition has practically no energy barrier [53]. In this model, the surface energy of the nuclei is negligible compared with their bulk free energy [54], thus spinodal decomposition can spontaneously occur and a phase separation takes place all over the reaction medium. The energetics of nonclassical nucleation are somewhere in between these two extremes of high energy barrier and no barrier [30, 55, 56]. In nonclassical nucleation, unlike what is assumed in classical nucleation theory, $\gamma$ and $\Delta G_{\mathrm{v}}$ are not constant with respect to particle size. Instead, there are intermediate structures with lower surface and/or bulk energy, which provide alternative pathways to circumvent the high energy barrier of homogeneous nucleation.

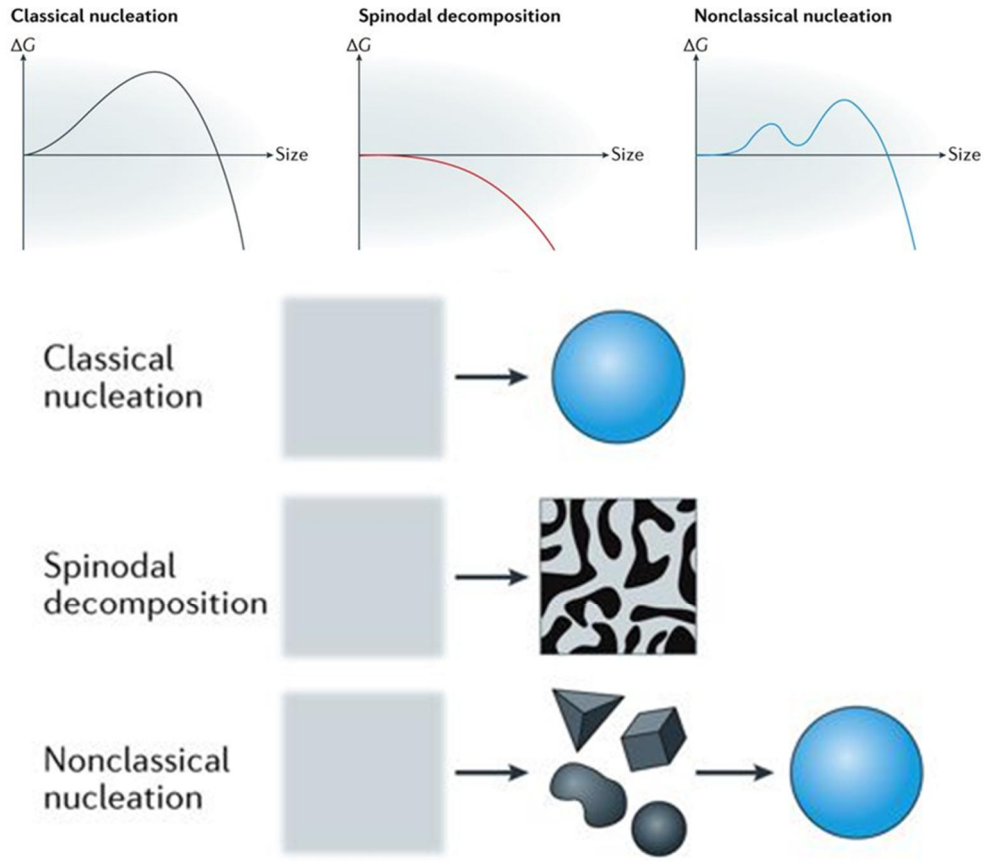


**Figure 1.2** Plots of free energy change as a function of nucleus size in the classical nucleation (left), spinodal decomposition (middle) and nonclassical nucleation (right) models.

### 1.3.2 Stepwise phase transitions

In addition to the geometric full-shell and electronic superatom configurations, which require specific conditions in terms of the number of atoms and electrons, other structural properties can stabilize prenucleation clusters, resulting in a decrease of the classical nucleation energy barrier. In particular, structural variances, such as amorphism and polymorphism, can contribute to the nonclassical nucleation pathway. Model studies of the 2D crystallization of colloidal microparticles and numerical simulations show that, under low supersaturation conditions, two-step nucleation through an amorphous-to-crystalline transition is energetically favoured over direct crystallization (classical nucleation) [57-61] (Figure 1.3a). In the first step, amorphous nuclei are formed — their surface energy is lower than that of crystalline nuclei as a consequence of their disordered interfaces with the solution. In the second step, an amorphous-to-crystalline transition takes place in the middle of the amorphous phase; this transition has to overcome a much lower free energy barrier compared with direct crystallization from solution. In other words, the amorphous phase can mediate the nucleation of the crystalline phase by buffering the large entropy difference between solution and crystal. Similarly, a

two-step nucleation mechanism has been observed in protein crystallization, in which crystalline nuclei are formed inside a metastable dense liquid phase [62].

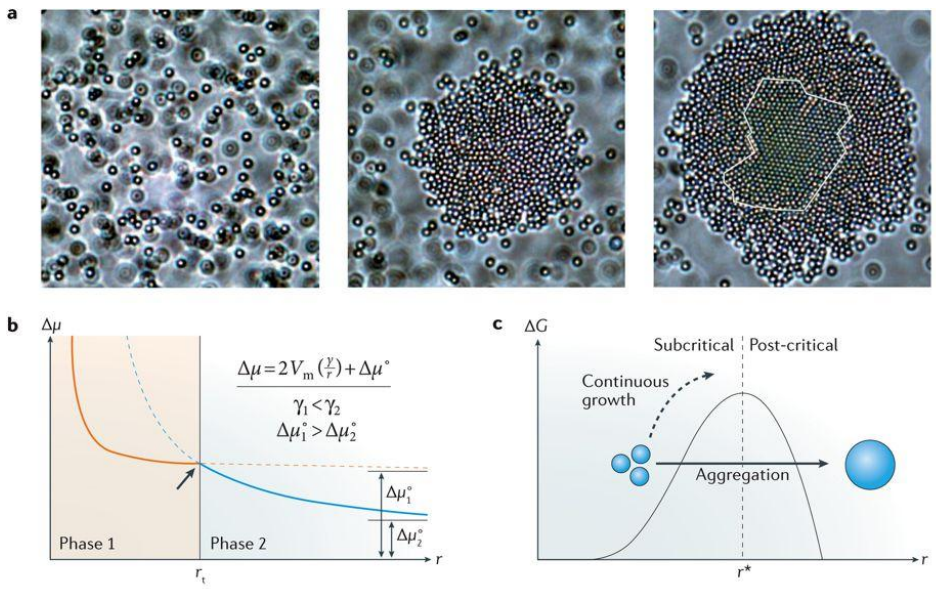


**Figure 1.3** Stepwise phase transitions and aggregation of nuclei. (a) Optical microscope images showing the multistep crystallization of colloidal polystyrene particles. A dilute liquid phase is initially observed (left), followed by an amorphous dense phase (middle) and by the formation of crystalline nuclei (right). (b) Chemical potential plots illustrating the transition from phase 1 (orange curve) to phase 2 (blue curve). (c) Nucleation by aggregation of prenucleation clusters. r*, critical radius. Panel a is adapted with permission from Ref. [57], American Chemical Society.

Stepwise phase transitions in the crystallization of polymorphic solids can also induce nonclassical nucleation [63-65]. In equation (1), when the particle is very small ($r << -3\gamma/\Delta G_v$), its free energy is dominated by the surface energy term ($4\pi r^2\gamma$). On the other hand, as the size of the particle increases, its thermodynamic stability becomes more dependent on the bulk free energy term ($4/3\pi r^3\Delta G_v$). As a result, in the initial stages, the nucleus tends to have the structure with the lowest surface energy but is transformed to the structure with the lowest bulk free energy as it grows, as conjectured in the Ostwald step rule [66]. For example, $ZrO_2$ nanoparticles have a tetragonal structure, whereas bulk $ZrO_2$ is monoclinic under ambient conditions [67, 68]. A stepwise phase transition occurring because of the difference between the surface and bulk energies of the two phases is illustrated in Figure 1.3b. The chemical potential function, $\Delta\mu(r)$, shown in the figure is derived from equation (1) using the relationship $\Delta\mu = [d(\Delta G_{hom})/dV] \times V_m$, where Vm is the molar volume and $\Delta\mu^o = \Delta G_v \times V_m$. When the particle radius is smaller than a value rt, phase 1, which has the lower surface energy ($\gamma_1$), is energetically favoured. However, as the size increases above $r_t$, a phase transition takes place at the cross point indicated by the arrow, after which phase 2, with lower bulk energy ($\Delta\mu_2^o$), becomes

more stable. Overall, in nucleation via amorphism and polymorphism, the nuclei are thermodynamically stabilized by their strong tendency to minimize their surface energy.

Structural disorder is observed in various nuclei and very small nanoparticles. In the 1980s, high resolution transmission electron microscopy studies revealed that various metal nanoparticles as small as a few nanometres are in a 'quasi-molten' state, in which their structure and shape are fluctuating from one state to another [69]. It was also theoretically shown that 1.4-nm-sized $Au_{55}$ clusters are more stable in the amorphous phase than when they form ordered structures [70]. In 2005, it was reported that the growth of CdSe nanoparticles 2 nm in size, consisting of ~160 atoms, is accompanied by crystallization and shape reconstruction of the nanoparticles, which are initially amorphous [71]. According to a detailed analysis of the structural disorder in 3.4-nm ZnS and 2–4-nm CdSe nanoparticles using atomic pair distribution function analysis [72, 73], these nanoparticles consist of a highly disordered shell and a crystalline core, resembling the crystalline core/amorphous shell structure of the condensed microparticles shown in Figure 1.3a. In the synthesis of CdTe nanoparticles with sizes <2 nm, a nucleation energy barrier lower

than that expected in the classical model was observed, which is attributed to the 'molten' state of the nanoparticles [74]. Transmission electron microscopy (TEM) studies of the early stage of the crystallization of minerals, including calcium carbonate, calcium phosphate and iron oxide, indicate that nucleation of these materials is initiated by the formation of amorphous nanoparticles that are transformed into crystalline nanoparticles during growth [54, 75-78]. Notably, nucleation from amorphous precursors is commonly observed in biological crystallization, in which cells actively transport and concentrate mineral ions to form the amorphous solid phase from which crystalline nuclei are formed [79]. Biomimetic model systems, including the polymer-induced liquid-precursor process, show a similar mechanism, in which an amorphous liquid-like phase or a dense liquid phase is formed first, and crystal nucleation takes place within it [80]. Overall, the formation of amorphous nuclei followed by a stepwise phase transition during growth is commonly observed in various reaction systems.

### 1.3.3 Aggregation of nuclei

Another important pathway of nonclassical nucleation is aggregation [30]. Compared with stepwise nucleation, which involves thermodynamic stabilization via structural change, the role of aggregation in the nucleation reaction has a more kinetic origin. As mentioned above, the subcritical nuclei with $r < r^*$ are unstable and supposed to dissolve. However, if their dissolution rate is much slower than their collision rate, it is possible that two or more subcritical nuclei bind together to form a stable post-critical nucleus ($r > r^*$) before total dissolution. Of course, this process does not only happen for the subcritical nuclei; stable nanoparticles can also aggregate to form larger ones, as we discuss in detail in the following section. Nevertheless, aggregation has a unique role in prenucleation and nucleation periods, because it makes the reaction system deviate far from the classical nucleation model [55, 81, 82]. Nucleation is a self-limiting process because the formation of nanoparticles lowers supersaturation and, as the supersaturation level decreases, part of the nuclei disappears by a ripening process [50]. Aggregation can stabilize the nuclei under ripening by abruptly increasing their size, which is equivalent to 'tunnelling' through the free energy barrier — this happens even at low

supersaturation, in which growth through atom-by-atom addition to reach the critical radius, r*, is not possible (Figure 1.3c). As a result, when the nanoparticle number concentration is high and supersaturation is low, aggregation can be the main nucleation pathway.

The development of liquid-cell TEMs has enabled the direct, real-time in situ observation of the aggregation of nanoparticles in solution [83-88]. An in situ measurement shows that the merging of 2 platinum nanoparticles and the subsequent shape reconstruction take place in timescales of hundreds of milliseconds and of less than 20 seconds, respectively [83, 86]. It was also found that there is a threshold nanoparticle number concentration below which aggregation does not occur [83]. High resolution electron tomography shows further evidence of the aggregation of nuclei [45, 89-93]. 3D atomic structures reconstructed using computed tomography reveal that a single metal nanoparticle is made of multiple crystal domains, which originate from the aggregation and merging of smaller nanoparticles in the early stages of the nanoparticle formation process [92].

In many cases, stepwise nucleation and aggregation work together in a complementary way. Easy formation of amorphous nanoparticles leads to a high number concentration and to more

frequent collisions among nanoparticles. Upon aggregation, the small amorphous nanoparticles, because of the abrupt size increase, reach the size regime in which the lower bulk energy is favoured (Figure 1.3b), and the amorphous-to-crystalline phase transition takes place. For example, during the precipitation of iron oxide in aqueous solution, amorphous prenucleation clusters of ~2 nm in size are formed first and subsequently aggregate into larger branched network structures [54]. As the reaction proceeds, crystalline nanoparticles 5–15 nm in size are formed from the denser part of the aggregates. Similar observations were made in the nucleation and growth of calcium phosphate, calcium carbonate and silica [75-77, 94-96].

## 1.4 Growth by assembly and merging

In classical crystallization theory, crystal growth is described as the addition of atoms or ions to the crystal lattice. This idea is expressed by the change of Gibbs free energy by crystallization, $\Delta G = kT \ln (a/a_o)$, where a and $a_o$ are the activity of the solute and bulk solid, respectively [49]. In reality, however, this classical model reflects only part of the picture. In the previous section, we discussed how aggregation of prenucleation clusters can contribute to the nucleation process. In a similar way, nanoparticle growth can proceed not only by atom-by-atom addition, but also by the assembly of smaller particles into larger particles [30, 48, 56, 97, 98]. The concept of crystal growth by assembly and merging of primary particles complements the classical theory by extending the definition of the building units from atoms and ions to clusters and nanoparticles. In this section, we examine emerging evidence for nonclassical crystal growth in the synthesis of various nanomaterials and discuss the mechanism behind the nanoparticle assembly and merging processes.

### 1.4.1 Oriented attachment

Oriented attachment is a well-recognized process for crystal growth from primary nanoparticles [99-103]. If two nanoparticles are attached to each other but their crystallographic orientations are not perfectly aligned parallel to each other, defects such as grain boundaries, twinning, or misfit dislocations are formed at the interface [99, 101]. However, in many nanostructures formed by the attachment of primary particles, it was observed that the primary particles are oriented so that they share the same crystal lattice and constitute a single domain [99, 102, 104-107] (Figure 1.4a). Considering that the probability of two colliding nanoparticles being perfectly oriented by chance is very low, this indicates that the crystal lattices of the nanoparticles become aligned, in some way, during attachment. Recent in situ liquid-cell TEM studies reveal that there are two underlying mechanisms in the assembly and merging processes (Figure 1.4b). First, if two nanoparticles are in close proximity before collision, then there is a strong interaction between them, favouring the alignment of their crystallographic orientations. This interaction is strong enough to induce the rotational and translational motions required to align the nanoparticles before collision. Once the alignment is complete, the

nanoparticles immediately merge together by an attractive force [83, 86, 103]. For semiconductor nanoparticles, such as CdS, CdTe and ZnS, it was suggested that this mutual alignment is induced by the dipole–dipole interaction between the nanoparticles [105, 106, 108]. However, this theory is not applicable to metal and other nanoparticles that have no permanent dipole moment, and the reason for their alignment has not yet been elucidated [83, 86]. Second, if two misaligned nanoparticles are attached, spontaneous reconstruction of the imperfect lattice takes place during the merging process to remove the defects [103]. Even after attachment, the nanoparticles can undergo multiple rotational motions to minimize the misalignment of their lattices (Figure 1.4c) [109]. These mechanisms show that the thermodynamic driving force for the reduction of the defect-free energy becomes significant at the nanometre scale, where it induces the lattice reconstruction and the motion of the primary particles.

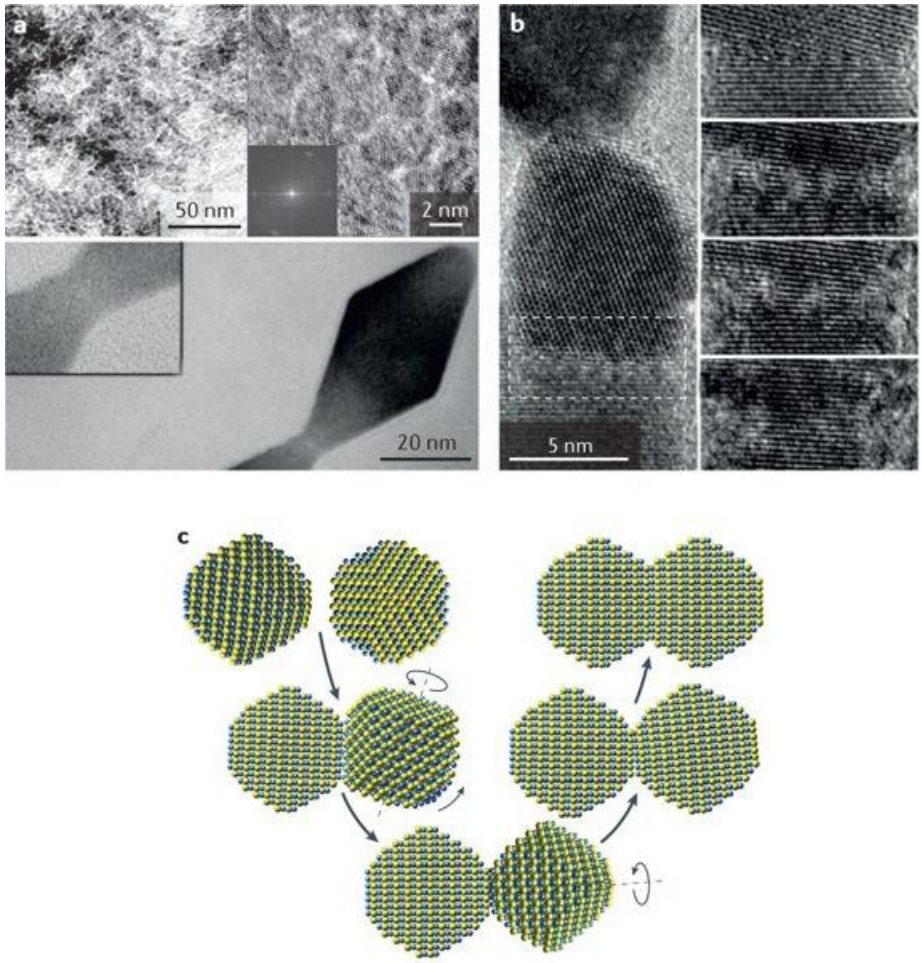


**Figure 1.4** Oriented attachment of nanoparticles. (a) Transmission electron microscopy (TEM) image of aggregated ferrihydrite nanoparticles (top). In the inset (right), a domain of aligned nanoparticles is magnified; the fast Fourier transform image shows that the nanoparticles share the same crystallographic axes. A TEM image of oriented attached titania nanoparticles is shown below. (b) Two

attached PbSe nanoparticles with slight lattice misalignment. The lattice structure changes at the interface with passing time from top to bottom (right) — the total intercurring time is 23 minutes. The number of dislocations decreases as the mistilt angle becomes zero; eventually the two particles become a single crystal. (c) Schematic representation of the rotational motion around three axes that a nanoparticle can perform to align its lattice with that of the nanoparticle it is attached to. Panel a is adapted with permission from Ref. [99], AAAS, and Ref. [102], Elsevier. Panels b and c are adapted with permission from Ref. [109], American Chemical Society.

The spontaneous alignment of approaching nanoparticles during oriented attachment reflects the complexity of interparticle interactions at the nanometre scale, which is not fully understood [110, 111]. In a recent Review article, various nonclassical behaviours of nanoparticle assemblies that are not consistent with the classical theory developed for colloidal microparticles were introduced [112]. It was shown that the assumptions made for microparticles to simplify the effects of solvent molecules, non-van der Waals interactions and the particle shape-dependent potentials cannot be extended to nanoparticles. At the nanometre scale, these effects become as important as those produced by the other forces, which makes the interactions between nanoparticles very difficult to analyse. Some interparticle interactions, which are negligibly weak at larger scales, such as the hydrophobic interaction of surface ligands, can have a significant role in nanoparticle assembly [113, 114]. As a consequence of the complexity of interparticle interactions, nanoparticle self-assembly often leads to unpredictable results, as in the case of quasicrystalline spherical nanoparticle superlattices [115, 116]. Usually, the self-assembly of spherical particles is an entropy-driven process that maximizes space-filling efficiency, which leads to the formation of Bravais lattice

structures with translational symmetry. However, quasicrystalline structures have no translational symmetry and cannot be understood in the frame of this entropy model.

In crystal growth by nanoparticle assembly, complex interparticle interactions can result in highly anisotropic nanostructures. Interestingly, different interactions can lead to very similar morphologies, as exemplified by the following three 2D nanostructures with differing compositions. First, it was reported that 3.4-nm-thick CdTe 2D nanosheets are formed by monolayer assembly of the primary CdTe nanoparticles160. In a simulation model study, it was shown that the truncated tetrahedral shape of CdTe nanoparticles and their unidirectional electric dipole moment are determinant for their 2D self-assembly (Figure 1.5a) [117, 118]. Second, in the synthesis of 2.2-nm-thick PbS nanosheets, it was observed that truncated cubic-shaped primary nanoparticles assemble into a nanosheet by preferential attachment of the highly reactive {110} facets, rather than through dipole–dipole interactions (Figure 1.5b) [119, 120]. Last, another 2D assembly mechanism was revealed in wurtzite CdSe nanostructures [121-124] that have a fixed thickness of 1.4 nm (Figure 1.5c). In this system, ligand-passivated $(CdSe)_{13}$ clusters assemble into lamellar

structures owing to the hydrophobic interaction between the ligands, and then the lamellar cluster assembly structures transform to CdSe nanocrystals [122, 124-128]. Interestingly, zinc blende CdSe nanosheets with thicknesses < 2 nm were synthesized using a classical crystal growth process instead of the primary particle assembly [129-132]. These examples illustrate the diversity of the nanoparticle assembly behaviours that can be used to build unique nanostructures.

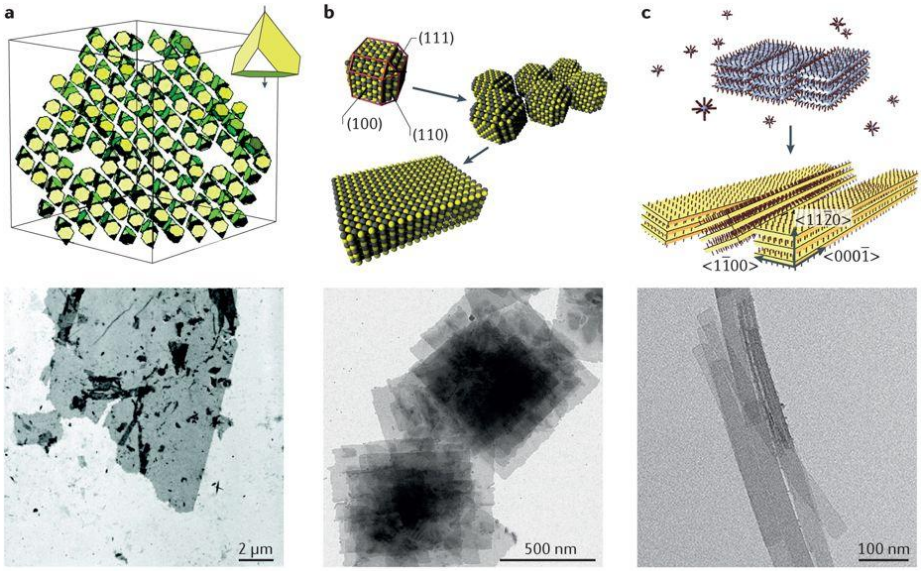


**Figure 1.5** Formation of 2D nanocrystals by assembly. (a) Simulation (top) of the 2D assembly of truncated tetrahedral CdTe nanoparticles, with the electric dipole moment indicated by the arrow and transmission electron microscopy (TEM) image of CdTe nanosheets (bottom). (b) Schematic representation (top) and TEM image (bottom) of PbS nanosheets formed by (110) attachment of PbS nanoparticles. (c) Schematic illustration showing the transformation of 2D lamellar assembly of $(CdSe)_{13}$ clusters (violet) into CdSe nanoribbons (yellow; top) and TEM image of CdSe nanoribbons (bottom). Panel a is adapted with permission from Ref. [118], American Chemical Society. Panel b is adapted with permission from Ref. [119], AAAS. Panel c (top) is adapted with permission from Ref. [126],

American Chemical Society.

As previously discussed, there is a strong tendency to align the lattices of two nanoparticles upon attachment, but there are some exceptions. Since the 1970s, it has been known that certain specific misalignments or 'twisting' are energetically favoured at the grain boundary of particles in contact [56, 133]. In 2015, the corresponding observation [92] of grain misalignment at the nanoscale was achieved by electron tomography of platinum nanoparticles smaller than 2 nm (Figure 1.6a). The tomogram shows that a single platinum nanoparticle consists of three domains that form twisted grain boundaries. The misalignment is induced to minimize the plane defect free energy at the grain boundary, where the (100) and (110) planes are in contact. The merging of the primary nanoparticles is also accompanied by morphological changes. The attachment of two nanoparticles results in a highly negative surface curvature around the contact point, which makes the structure energetically unstable [134]. The surface tension results in a tendency to minimize the net surface area, inducing mass transport to fill the region around the contact point [86]. When PbSe nanoparticles are attached through their {100} facets, they are elongated in a direction parallel to their bonding axis to form a 'neck' around their contact point [135]. In the unidirectional attachment of

$Pt_3Fe$ nanoparticles to form nanorods, a macroscopic reconstruction takes place to straighten the initially rugged surface, as well as to align the lattices of the particles (Figure 1.6b) [87]. The presence of the surface ligands on the nanoparticles can be an effective barrier for attachment, thus ligand removal is sometimes necessary [136]. In addition, it is possible that the mass transport of atoms during merging contributes to the removal of the ligands from the contact region [135]. Rather than being totally removed, it was suggested that the ligand molecules are transported by making them 'jump' from one binding site to the next on the surface of the nanoparticle, which requires less energy than desorption [137].

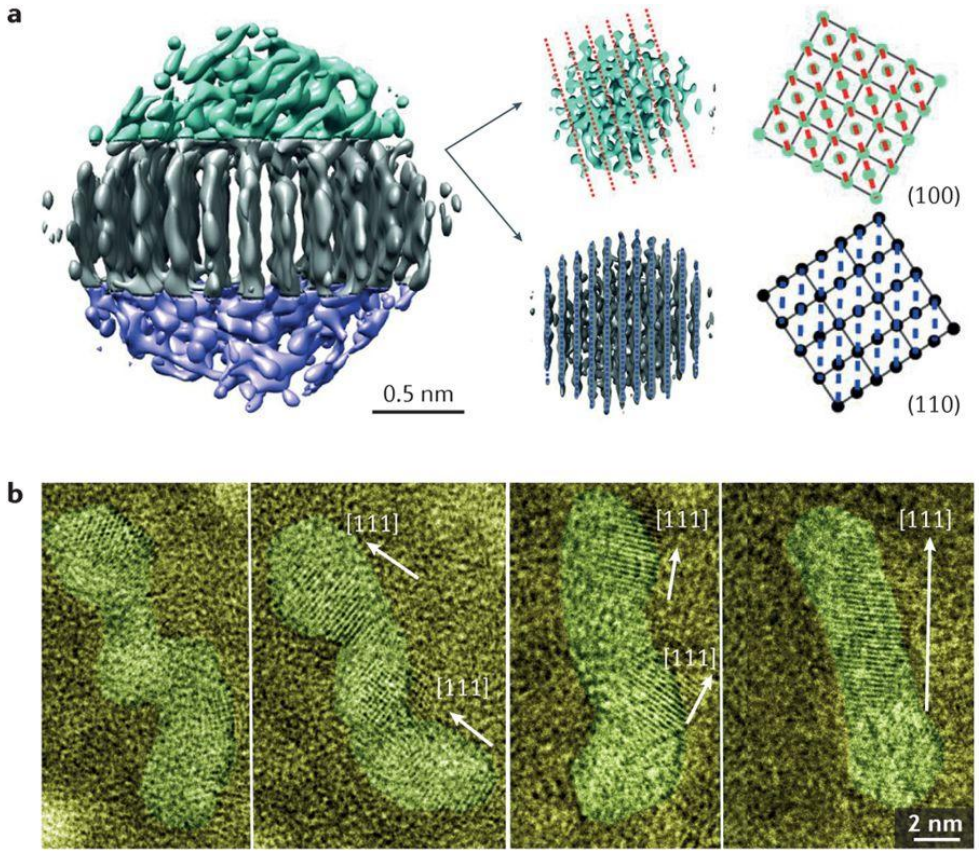


**Figure 1.6** Multidomain structures of nanoparticles. (a) Electron tomogram of a face-centred cubic platinum nanoparticle consisting of three domains (left). Cross sectional views of the grain boundary between the upper and the middle domains are shown on the right. The (100) plane of the upper domain and the (110) plane of the middle domain meet with a rotation angle of 14°. The angle is measured with respect to {111} planes, indicated in red and blue dash lines for the upper and middle domain, respectively. (b) Transmission electron

microscopy images show the fusion of three $Pt_3Fe$ particles into a single crystal. From left to right, the crystal orientation changes with atomic redistribution and eventually the crystal shape changes to form a single domain nanorod. Panel a is adapted with permission from Ref. [92], AAAS. Panel b is adapted with permission from Ref. [87], AAAS.

### 1.4.2 Mesocrystals formation

The assembly of primary nanoparticles can also lead to the formation of mesocrystals, in which the nanoparticles remain as individual building units instead of merging into a single crystal domain [56, 97, 138, 139]. As a result, mesocrystals have both lattice structures at the atomic scale and secondary structures at the nanometre scale. Mesocrystals are widely observed not only as a result of the assembly of synthesized inorganic nanoparticles, but also in biominerals such as skeletons and shells [138]. Typically, mesocrystals consist of inorganic nanoparticles and of an organic phase filling the space between the nanoparticles; such unique hybrid structures provide the possibility to control their physicochemical and mechanical properties [139]. In addition, mesocrystals can be regarded as intermediate states in the transition from primary nanoparticles to single-domain crystals via assembly and merging [107, 140]. For this reason, we expect that kinetic studies on the transformation of mesocrystals into single-domain crystals will provide important information on the merging process of primary nanoparticles with different surface ligands and grain boundaries.

In a classical perspective, crystallization is a direct transition

from atomic building units to crystals. However, the nucleation and growth processes discussed so far reveal that multiple intermediate steps are involved in the transition [141]. In nonclassical pathways, crystallization proceeds from atoms to nanoclusters, to nanoparticles, to mesocrystals, and finally to bulk crystal solids. In this process, the product of each step becomes the building unit for the next, which is characteristic of nonclassical crystallization.

## 1.5 Heterogeneous nucleation

### 1.5.1 Heterogeneous nucleation process

Heterogeneous nucleation takes place in a heterogeneous reaction medium that contains the nucleation seeds. In the synthesis of multicomponent nanoparticles, heterogeneous nucleation is of great importance. By inducing the formation of a secondary phase at the surface of the seed nanoparticles, this process enables the synthesis of a surprisingly wide variety of multicomponent nanostructures [6, 7, 26-29, 142, 143]. However, our current understanding of heterogeneous nucleation at the nanometre scale is far from complete. The mechanism behind the synthetic methods that are based on heterogeneous nucleation is substantially different from that governing the formation of single-component nanoparticles, therefore its study requires new techniques and theoretical frameworks. In this section, we briefly discuss the heterogeneous nucleation theory and examine various nucleation behaviours of multicomponent nanoparticles.

In the heterogeneous nucleation process, a nucleus formed at the surface of a seed can be stabilized by the interface with the seed, which radically changes the energetics of the nucleation reaction

compared with that of homogeneous nucleation. To calculate the Gibbs free energy change of heterogeneous nucleation, $\Delta G_{het}$, we assume that a nucleus with a critical radius, r*, is formed at the surface of a spherical seed with radius R (Figure 1.7a). The interface energy, $\gamma_i$, of the nucleus and the seed is related to the nucleus–seed contact angle, $\theta_c$, through Young's equation, $\cos\theta_c = (\gamma_s - \gamma_i)/\gamma$, where $\gamma_s$ and $\gamma$ are the surface energy of the seed and the nucleus, respectively. The value of $\Delta G_{het}$ can be written [144] as a function of x = R/r* and m =cos $\theta_c$ as:

$$\Delta G_{ht} = \frac{8\pi\gamma^3 V_m^2}{3\left[RT\ln\left(\frac{a}{a_o}\right)\right]^2} \cdot h(m,x) \tag{2}$$

where

$$h(m,x) = 1 + \left(\frac{1-mx}{g}\right)^3 + x^3\left[2 - 3\left(\frac{x-m}{g}\right) + \left(\frac{x-m}{g}\right)^3\right] + 3mx^2\left(\frac{x-m}{g} - 1\right) \tag{3}$$

and

$$g = \sqrt{1 + x^2 - 2mx} \tag{4}$$

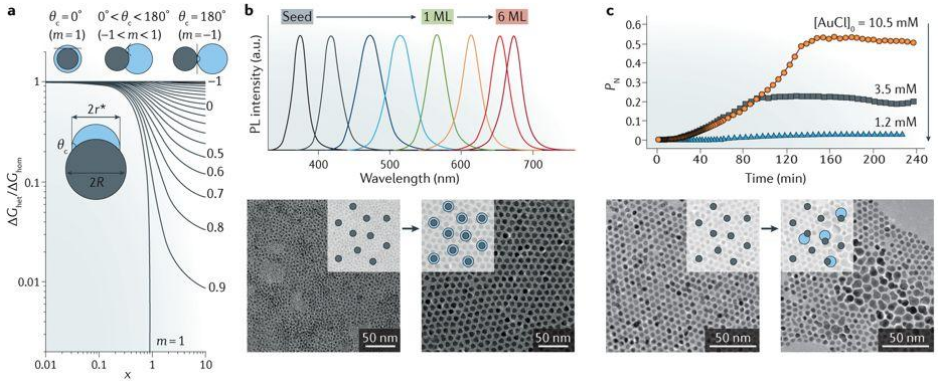


**Figure 1.7** Energetics and nucleation probability of heterogeneous nucleation. (a) Plots of the Gibbs free energy change for heterogeneous nucleation, $\Delta G_{het}$, for a nucleus with a spherical surface of curvature radius r*. The values of $\Delta G_{het}$ calculated from equation (2) are normalized by the Gibbs free energy change for homogenous nucleation, $\Delta G_{hom}$, and plotted against $x = R/r^*$ for various values of $m = \cos\theta_c$, where R is the radius of a spherical seed and $\theta_c$ is the contact angle. (b) Temporal evolution of normalized photoluminescence (PL) spectra of ZnSe–CdSe core–shell nanoparticles during shell formation (top). As the shell thickness increases, the emission peak position is red shifted, whereas the shape and width of the peaks are relatively constant. As the peak shape roughly reflects the size distribution of the nanoparticles (a narrow peak indicates a uniform size distribution), these data indicate the formation of a uniform shell on all seed

nanoparticles. Transmission electron microscopy (TEM) images of ZnSe seeds and ZnSe–CdSe core–shells with a shell thickness of 6 monolayers (MLs) (bottom). (c) Nucleation probability, PN, as a function of reaction time for $CoPt_3$–Au nanodumbbells synthesized with different concentrations of the gold precursor (AuCl) (top). TEM images of the nanoparticles before and after the reaction of $CoPt_3$ seeds in a AuCl solution with a concentration of 10.5 mM (bottom). Panel b is adapted with permission from Ref. [145], American Chemical Society. Panel c is from Ref. [146], Nature Publishing Group.

When there is no seed (R = 0), equation (2) becomes identical to the Gibbs free energy for homogeneous nucleation, $\Delta G_{hom}(r^*)$ (equation (1)). As the contact angle decreases from $180^o$ (which corresponds to a nucleus and seed in contact only at one point), the nucleus becomes more stable with respect to $\Delta G_{hom}$, and eventually the energy barrier goes to 0 when m = 1 ($\theta_c = 0^o$ is realized when the nucleus envelops the seed, Figure 1.7a).

When measuring the heterogeneous nucleation kinetics, it is convenient to use a parameter called nucleation probability, $P_n = N_n/N_{tot}$, where $N_n$ and $N_{tot}$ are the number of seeds that have nuclei and the total number of seeds, respectively [147, 148]. On the basis of the classical model shown in Figure 1.7a, we would expect that the nucleation probability of core–shell nanoparticles, for which the contact angle is $0^o$ (m = 1), is ~100 % because the energy barrier for the shell formation is practically 0 due to the low interface energy. This is confirmed by data from the synthesis of semiconductor core–shell nanoparticles [145, 149]. Photoluminescence spectra (Figure 1.7b) show that when the seed nanoparticles react in solution with the precursors of the shell material they are all converted into core–shell structures through heterogeneous nucleation and growth of the shell on their surface. By contrast, when

the shape of the heterostructures is dumbbell-like, the nucleation probability becomes strongly dependent on the precursor concentration. In the reaction of $CoPt_3$ seed nanoparticles with a gold precursor, for example, the nucleation probability of $CoPt_3$–Au nanodumbbells rapidly decreases from 52 % to near 0 % as the precursor concentration decreases (Figure 1.7c) [146]. In this case, the interface energy between $CoPt_3$ and Au is relatively high, so that the contact angle is larger than 0 ($m < 1$). As a result, the energy barrier, $\Delta G_{het}$, can effectively block the heterogeneous nucleation and the nuclei can form only on part of the seeds (Figure 1.7c). In general, the interface energy is the main factor that determines the shape of the nucleus in heterogeneous nucleation [142, 143], as well as the height of the energy barrier of the nucleation reaction.

### 1.5.2 Interface energy minimization and property tuning by lattice strain

In the section on homogeneous nucleation, we mentioned that the tendency to reduce the surface energy results in nonclassical nucleation behaviours. Correspondingly, in heterogeneous nucleation, there is a strong tendency to minimize the interface energy of the nucleus and the seed. If the nucleus and the seed form a heteroepitaxial interface, the interface energy increases with their lattice mismatch. As a result, their lattices are mechanically strained to reduce the mismatch at the interface. For example, in the synthesis of $CoPt_3$–Au nanodumbbells mentioned above, it was observed that the lattice of the $CoPt_3$ seeds is strained by a stress of 2.4 GPa when the gold phase nucleates on their surface [146]. This happens because both $CoPt_3$ and Au have a fcc structure, but their lattice mismatch is 5.3 %. For wurtzite CdS–ZnS core–shell nanoparticles, which have a lattice mismatch of 7 %, a stress of > 4 GPa was observed for shells with a thickness of 7.5 monolayers [150]. Lattice strain in the overgrowth phase to remove the mismatch with the substrate lattice is commonly observed in heteroepitaxial thin film growth, a phenomenon known as pseudomorphism (Figure 1.8a) [151, 152]. However, unlike thin film

substrates, seed nanoparticles have very small finite sizes, thus the restoration force from the strained overgrowth phase can induce deformation of the seed, so that the forces in the seed and in the overgrowth phase are in equilibrium (Figure 1.8b). As shown in the case of $CoPt_3$–Au nanodumbbells and CdS–ZnS core–shells, the mechanical stress induced by the formation of a heteroepitaxial interface can be very high. From the synthetic point of view, this behaviour can be exploited to control the lattice of the multicomponent nanoparticles by selecting seeds and overgrowth phases with appropriate lattice mismatch and elastic moduli.

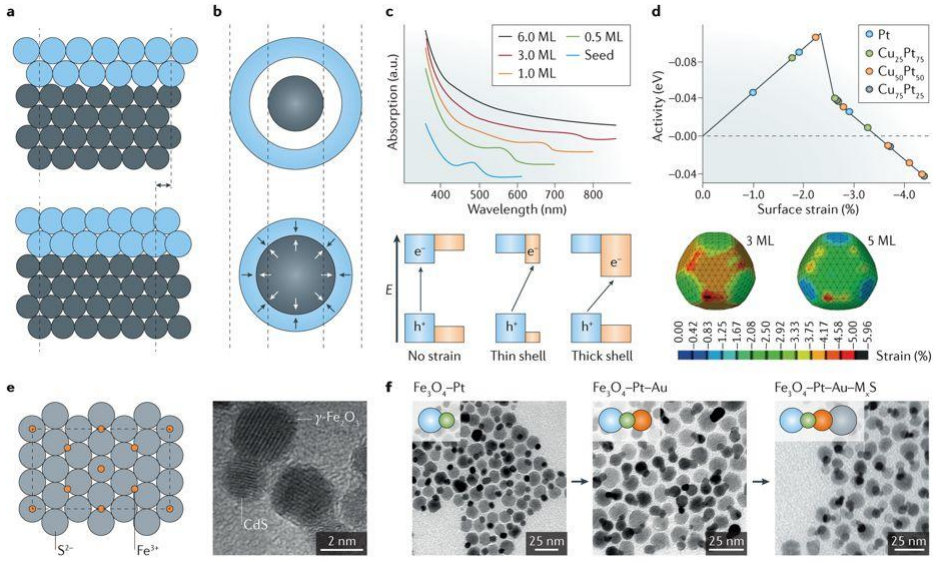


**Figure 1.8** Lattice strain and structural properties of multicomponent nanoparticles. (a) Schematic illustrations of an unstrained overgrowth layer (blue; top) and of a pseudomorphic layer (bottom) on the substrate (grey). (b) Unstrained core and shell (top) and strained core–shell structure (bottom). The arrows indicate the direction of the radial stress in the core and in the shell. (c) Absorption spectra of CdTe–ZnSe core–shell nanoparticles with different shell thicknesses and corresponding band diagrams. As the shell thickness increases, negative and positive strain is induced in the core and the shell, respectively. This leads to a conversion of the band structure from type I to type II, as illustrated in the sketch below and as indicated by the red shift of the absorption peak position. (d) Plot for the catalytic activity of

platinum for the oxygen reduction reaction as a function of the surface strain of platinum atoms (top). Circles with different colours show the activity of simulated Cu–Pt/Pt core–shell nanoparticles with a shell thickness of 3–5 monolayers (MLs). Simulation of surface strain for 3 and 5 ML-thick platinum shells on a 5 nm $Cu_{50}Pt_{50}$ core (bottom). (e) Coincidence site (dashed box) of the interface between the γ-$Fe_2O_3$ (111) and the zinc blende CdS (111) planes. The $Fe^{3+}$ lattice is expanded by 4.6 % to remove the mismatch with the S2− lattice. The transmission electron microscopy (TEM) image shows γ-$Fe_2O_3$–CdS nanodumbbells. (f) Schematic illustrations and TEM images showing sequential synthesis of Pt–Fe3O4 heterodimers, Pt–$Fe_3O_4$–Au heterotrimers and Pt–$Fe_3O_4$–Au–$Cu_9S_5$ heterotetramers. Panel c is from Ref. [153], Nature Publishing Group. Panel d is adapted with permission from Ref. [154], American Chemical Society. Panel e is adapted with permission from Ref. [155], American Chemical Society. Panel f is from Ref. [156], Nature Publishing Group.

The idea of adjusting the lattice constant to modify the physicochemical properties of nanoparticles has been demonstrated both experimentally and theoretically. In general, lattice strain in semiconductors induces changes in the bandgap energy and in the charge carrier mobility. Using this property, the bandgap offset of semiconductor nanoparticles with heteroepitaxial core–shell structures can be modified [153]. By encapsulating 'soft' (low elastic modulus) CdTe cores with a shell of other II–VI semiconductors with smaller lattice constants, compressive stress in the core and extensional stress in the shell can be induced simultaneously. As the relative strain in the core and in the shell is determined by the shell thickness, the band alignment can be transformed from type I to type II, as indicated by optical absorption spectra (Figure 1.8c). In addition, it was shown by theoretical simulations that the mechanical stress within the core–shell structure can make a high-pressure phase stable at ambient pressure. For example, for bulk CdSe, the rocksalt structure is stable only under a pressure of ~2 GPa. By contrast, in a simulation of CdSe–ZnS core–shell nanoparticles, if the nanoparticle is subjected to a pressure of 20 GPa, the rocksalt CdSe core remains metastable even after the external pressure is removed [157]. Similarly, in another simulation model, it

was shown that rocksalt CdSe can be stabilized under atmospheric pressure in a ZnS–CdSe–ZnS core–shell–shell structure because of heteroepitaxial lattice strain [158]. Lattice tuning is also relevant for the synthesis of nanoparticles with improved electrocatalytic activity. According to density functional theory calculations, there is an optimum lattice strain of platinum that results in enhanced catalytic activity in the oxygen reduction reaction compared with unstrained platinum [154, 159, 160]. A simulation of the catalytic activity of $Cu_xPt_{(1-x)}$–Pt core–shell nanostructures, in which the strain was continuously adjustable in the range between −4.5 % and 0 % by controlling the ratio of copper and platinum in the core [154], is shown in Figure 1.8d. It was also experimentally confirmed that Cu–Pt-alloy core/lattice-strained-Pt shell nanoparticles have high catalytic activity compared with pristine platinum nanoparticles [159]. A similar approach of lattice strain tuning to enhance the catalytic activity was reported for FePt–Pt core–shell nanoparticles [160].

Obviously, having similar crystal structures is not a necessary condition for heterogeneous nucleation, and there are other ways to lower the interface energy between seeds and nuclei. Among them, the coincidence site lattice model explains the cases in which two different

crystal structures have a coherent interface [161, 162]. In Figure 1.8e, for example, the (111) planes of γ-$Fe_2O_3$ and zinc blende CdS are shown together. Although their 3D structures have little resemblance, the 2D lattices of $Fe^{3+}$ and $S^{2-}$ on the (111) plane can be overlapped with a small lattice mismatch of 4.6 %. As a result, γ-$Fe_2O_3$–CdS nanodumbbells can be synthesized through the formation of a (111)/(111) interface [155]. Note that, since the zinc blende CdS (111) plane and the wurtzite CdS (001) plane are equivalent, wurtzite CdS nanoparticles are also formed via the CdS(001)/γ-$Fe_2O_3$(111) interface. An interface of coincidence lattices can be formed not only between well-defined facets, but also between curved surfaces, as exemplified by the formation of γ-$Fe_2O_3$ nanoparticles at the tip of bent $TiO_2$ nanorods [163]. High chemical affinity is another important factor that facilitates heterogeneous nucleation. Owing to the strong chemical bonds between noble metals (gold, silver and platinum) and chalcogens (sulfur, selenium and tellurium), it is easy to induce the deposition of either metals on the surface of chalcogenide nanoparticles or chalcogens on the surface of metal nanoparticles. Using this approach, various nonepitaxial multicomponent nanostructures, including gold-tipped CdSe nanorods [164, 165], Au–CdS core–shell nanoparticles

[166] and FePt–CdS nanodumbbells [167], have been prepared. Furthermore, it was demonstrated that by using chemoselective deposition of metals and metal sulfides, heterotrimers and heterotetramers can be prepared by using Pt–$Fe_3O_4$ nanodumbbells as seeds [156]. As shown in Figure 1.8f, if a gold precursor is reacted with Pt–$Fe_3O_4$ heterodimers, gold nanoparticles exclusively nucleate on the surface of platinum. Then, the reaction of the heterotrimers with metal and sulfur precursors leads to the formation of metal sulfide nanoparticles attached to only gold nanoparticles to form linear heterotetramers.

Finally, it is also reported that coincidence lattices and chemical affinity can work in a complementary way to lead to the formation of low-energy interfaces. In the case of $UO_2$–$In_2O_3$ and FePt–$In_2O_3$ nanodumbbells, the lattice of $In_2O_3$ is strained so that the interfaces are coherent [168]; however, the preferred nucleation sites on the seeds are not the facets with the minimum lattice mismatch but the ones with the strongest chemical affinity.

## 1.6 Conclusions

The rapid development of nanochemistry has been, so far, largely sustained by knowledge coming from various traditional research areas. In the early times of the field, scientists working in nanochemistry tried to explain their observations using well-established classical theories. For example, many of the synthetic reactions for the formation of nanoparticles were adopted from organometallic and sol–gel chemistry. The main concepts behind the formation mechanisms of monodisperse nanoparticles are direct extensions of the classic theory of colloidal chemistry, such as bursts of nucleation described by the LaMer diagram. Nowadays, as nanochemistry becomes a mature field, nonclassical phenomena that are unique to nanoscale materials are attracting an increasing amount of interest. In this Review, we discussed nucleation and growth mechanisms in nanoparticle synthesis that are not consistent with the classical crystallization theory. As we briefly mentioned in the introduction, the study of nonclassical crystallization of nanoparticles is of pivotal importance to establish a fundamental understanding of nanochemistry and to provide technical solutions for various applications of nanomaterials.

With increasing evidence of nonclassical crystallization behaviours at the nanoscale, the modification of some aspects of the traditional crystallization theory is strongly required. Multistep nucleation and the formation of nanoclusters in the prenucleation period can make the reaction system deviate from the one predicted by classical nucleation theory, which assumes a single-step transition from solute to solid. At the moment, however, experimental data on the prenucleation and nucleation periods of the nanoparticle formation are still limited, which hampers the development of more realistic theoretical models. Despite the technical difficulties in monitoring sub- and few-nanometre sized objects, a number of significant contributions have been made using in situ TEM, X-ray scattering and optical spectroscopy techniques. With the continuous development of characterization techniques, it is expected that more detailed information on the kinetics and on the structural changes in the prenucleation and nucleation periods will be available soon.

The formation of diverse intermediate structures between atoms and crystalline solids, which include nanoclusters, nanoparticles and mesocrystals, changes the traditional view of crystallization. Instead of the direct assembly of atoms into crystalline lattices, the

intermediate structures in nonclassical crystallization show various assembly and aggregation behaviours at different scales, from subnanometre up to tens of nanometres. Sometimes those behaviours lead to anisotropic crystal growth or superlattice structure formation, adding much more complexity to crystal structures than what would be expected from classical crystallization theory. We expect that future studies on multiscale assembly mechanisms will give valuable insight into material self-organization, as in the case of biomineralization.

The importance of the synthesis of multicomponent nanoparticles with desired interfaces and morphologies is rapidly increasing due to the technical requirements for applications, such as catalytic activity and efficient charge and mass transport. As mentioned above, nonclassical crystallization studies provide an effective framework for the understanding and control of the structural complexity of nanomaterials. In particular, the study of heterogeneous nucleation mechanisms of multicomponent nanoparticles is needed to understand the energetics of the interface formation and of structural changes during synthesis. We believe that the study of nanochemistry will not only contribute to fundamental science, but will also form the basis of a systematic approach for the synthesis of complex

nanostructures with improved performance.

Most of the contents of this chapter were published in the article "Nonclassical nucleation and growth of inorganic nanoparticles" (*Nature Reviews Materials* **2016**, 1, 16034).

## 1.7 References


[1] Murray, C. B.; Norris, D. J.; Bawendi, M. G. *J. Am. Chem. Soc.* **1993,** 115, 8706-8715.

[2] Rogach, A. L. *Adv. Funct. Mater.* **2002,** 12, 653-664.

[3] Yin, Y.; Alivisatos, A. P. *Nature* **2005,** 437, 664-670.

[4] Park, J.; Joo, J.; Kwon, S. G.; Jang, Y.; Hyeon, T. *Angew. Chem. Int. Ed. Engl.* **2007,** 46, 4630-4660.

[5] Talapin, D. V.; Lee, J. S.; Kovalenko, M. V.; Shevchenko, E. V. *Chem. Rev.* **2010,** 110, 389-458.

[6] Carbone, L.; Cozzoli, P. D. *Nano Today* **2010,** 5, 449-493.

[7] Donegá, C. d. M. *Chem. Soc. Rev.* **2011,** 40, 1512-1546.

[8] Kovalenko, M. V. *Acs Nano* **2015,** 9, 1012-1057.

[9] Cleveland, C. L. *Phys. Rev. Lett.* **1997,** 79, 1873-1876.

[10] Kubo, R.; Kawabata, A.; Kobayashi, S. *Annu. Rev. Mater. Sci.* **1984,** 14, 49-66.

[11] Alivisatos, A. P. *Science* **1996,** 271, 933-937.

[12] Kim, J. Y.; Kotov, N. A. *Chem. Mater.* **2014,** 26, 134-152.

[13] Shirasaki, Y.; Supran, G. J.; Bawendi, M. G.; Bulovic´, V. *Nat. Photonics* **2013,** 7, 13-23.

[14] Choi, M. K. *Nat. Commun.* **2015,** 6, 7149.

[15] Atwater, H. A.; Polman, A. *Nat. Mater.* **2010,** 9, 205-213.

[16] Barnes, W. L.; Dereux, A.; Ebbesen, T. W. *Nature* **2003,** 424, 824-830.

[17] Carey, G. H. *Chem. Rev.* **2015,** 115, 12732-12763.

[18] Armand, M.; Tarascon, J. M. *Nature* **2008,** 451, 652-657.

[19] Aricò, A. S.; Bruce, P.; Scrosati, B.; Tarascon, J. M.; Schalkwijk, W. V. *Nat. Mater.* **2005,** 4, 366-377.

[20] Guo, S.; Zhang, S.; Sun, S. *Angew. Chem. Int. Ed. Engl.* **2013,** 52, 8526-8544.

[21] Somorjai, G. A.; Park, J. Y. *Angew. Chem. Int. Ed. Engl.* **2008,**

47, 9212-9228.

[22] Somorjai, G. A.; Contreras, A. M.; Montano, M.; Rioux, R. M. *Proc. Natl Acad. Sci. Usa* **2006,** 103, 10577-10583.

[23] Giljohann, D. A.; Mirkin, C. A. *Nature* **2009,** 462, 461-464.

[24] Lee, N. *Chem. Rev.* **2015,** 115, 10637-10689.

[25] Medintz, I. L.; Uyeda, H. T.; Goldman, E. R.; Mattoussi, H. *Nat. Mater.* **2005,** 4, 435-446.

[26] Costi, R.; Saunders, A. E.; Banin, U. *Angew. Chem. Int. Ed. Engl.* **2010,** 49, 4878-4897.

[27] Goesmann, H.; Feldmann, C. *Angew. Chem. Int. Ed. Engl.* **2010,** 49, 1362-1395.

[28] Buck, M. R.; Schaak, R. E. *Angew. Chem. Int. Ed. Engl.* **2013,** 52, 6154-6178.

[29] Wang, C.; Xu, C.; Zeng, H.; Sun, S. *Adv. Mater.* **2009,** 21, 3045-3052.

[30] Wang, F.; Richards, V. N.; Shields, S. P.; Buhro, W. E. *Chem.*

*Mater.* **2014,** 26, 5-21.

[31] Billinge, S. J. L. *Physics* **2010,** 3, 25.

[32] Sugimoto, T. *Adv. Colloid Interfac. Sci.* **1987,** 28, 65-108.

[33] Zheng, J.; Zhang, C.; Dickson, R. M. *Phys. Rev. Lett.* **2004,** 93, 77402.

[34] Sadeghi, O.; Zakharov, L. N.; Nyman, M. *Science* **2015,** 347, 1359-1362.

[35] Miller, J. S.; Drillon, M., *Magnetism: Molecules to materials III: Nanosized Magnetic Materials*. Wiley-VCH: 2002.

[36] Qian, H.; Zhu, M.; Wu, Z.; Jin, R. *Acc. Chem. Res.* **2012,** 45, 1470-1479.

[37] Häkkinen, H. *Chem. Soc. Rev.* **2008,** 37, 1847-1859.

[38] Schmid, G. *Chem. Soc. Rev.* **2008,** 37, 1909-1930.

[39] Heaven, M. W.; Dass, A.; White, P. S.; Holt, K. M.; Murray, R. W. *J. Am. Chem. Soc.* **2008,** 130, 3754-3755.

[40] Akola, J.; Walter, M.; Whetten, R. L.; Häkkinen, H.; Grönbeck, H. *J. Am. Chem. Soc.* **2008,** 130, 3756-3757.

[41] Häkkinen, H. *Nat. Chem.* **2012,** 4, 443-455.

[42] Zhu, M.; Aikens, C. M.; Hollander, F. J.; Schatz, G. C.; Jin, R. *J. Am. Chem. Soc.* **2008,** 130, 5883-5885.

[43] Jadzinsky, P. D.; Calero, G.; Ackerson, C. J.; Bushnell, D. A.; Kornberg, R. D. *Science* **2007,** 318, 430-433.

[44] Walter, M. *Proc. Natl Acad. Sci. Usa* **2008,** 105, 9157-9162.

[45] Azubel, M. *Science* **2014,** 345, 909-912.

[46] Larson, R. B. *Rep. Prog. Phys.* **2003,** 66, 1651-1697.

[47] Whitesides, G. M.; Grzybowski, B. *Science* **2002,** 295, 2418-2421.

[48] De Yoreo, J. J. *Science* **2015,** 349, aaa6760.

[49] Mullin, J. W., *Crystallization*. Butterworth-Heinemann: 2001.

[50] Kwon, S. G.; Hyeon, T. *Small* **2011,** 7, 2685-2702.

[51] Kwon, S. G. *J. Am. Chem. Soc.* **2007,** 129, 12571-12584.

[52] LaMer, V. K.; Dinegar, R. H. *J. Am. Chem. Soc.* **1950,** 72, 4847-4854.

[53] Cahn, J. W. *Acta Mater.* **1961,** 9, 795-801.

[54] Baumgartner, J. *Nat. Mater.* **2013,** 12, 310-314.

[55] Watzky, M. A.; Finke, R. G. *J. Am. Chem. Soc.* **1997,** 119, 10382-10400.

[56] Fang, J.; Ding, B.; Gleiter, H. *Chem. Soc. Rev.* **2011,** 40, 5347-5360.

[57] Zhang, T. H.; Liu, X. Y. *J. Am. Chem. Soc.* **2007,** 129, 13520-13526.

[58] Zhang, T. H.; Liu, X. Y. *Angew. Chem. Int. Ed. Engl.* **2009,** 48, 1308-1312.

[59] Zhang, T. H.; Liu, X. Y. *J. Phys. Chem. B* **2007,** 111, 14001-14005.

[60] Savage, J. R.; Dinsmore, A. D. *Phys. Rev. Lett.* **2009,** 102, 198302.

[61] Wolde, P. R. t.; Frenkel, D. *Science* **1997,** 277, 1975-1978.

[62] Vekilov, P. G. *Nanoscale* **2010,** 2, 2346-2357.

[63] Navrotsky, A. *Proc. Natl Acad. Sci. Usa* **2004,** 101, 12096-12101.

[64] Navrotsky, A. *Chem Phys Chem* **2011,** 12, 2207-2215.

[65] Zhang, H.; Banfield, J. F. *J. Phys. Chem. B* **2000,** 104, 3481-3487.

[66] Van Santen, R. A. *J. Phys. Chem.* **1984,** 88, 5768-5769.

[67] Garvie, R. C. *J. Phys. Chem.* **1978,** 82, 218-224.

[68] Joo, J. *J. Am. Chem. Soc.* **2003,** 125, 6553-6557.

[69] Marks, L. D. *Rep. Prog. Phys.* **1994,** 57, 603-649.

[70] Garzón, I. L.; Posada-Amarillas, A. *Phys. Rev. B* **1996,** 54, 11796-11802.

[71] Chen, X.; Samia, A. C. S.; Lou, Y.; Burda, C. *J. Am. Chem. Soc.* **2005,** 127, 4372-4375.

[72] Gilbert, B.; Huang, F.; Zhang, H.; Waychunas, G. A.; Banfield, J. F. *Science* **2004,** 305, 651-654.

[73] Masadeh, A. S. *Phys. Rev. B* **2007,** 76, 115413.

[74] Piepenbrock, M. O. M.; Stirner, T.; O'Neill, M.; Kelly, S. M. *J. Am. Chem. Soc.* **2007,** 129, 7674-7679.

[75] Gebauer, D.; Völkel, A.; Cölfen, H. *Science* **2008,** 322, 1819-1822.

[76] Pouget, E. M. *Science* **2009,** 323, 1455-1458.

[77] Laven, J. *Nat. Commun.* **2013,** 4, 1507.

[78] Wang, L.; Nancollas, G. H. *Chem. Rev.* **2008,** 108, 4628-4669.

[79] Weiner, S.; Addadi, L. *Annu. Rev. Mater. Res.* **2011,** 41, 21-40.

[80] Gower, L. B. *Chem. Rev.* **2008,** 108, 4551-4627.

[81] Wang, Z.; Wang, F.; Peng, Y.; Zheng, Z.; Han, Y. *Science* **2012,**

338, 87-90.

[82] Huang, F.; Zhang, H.; Banfield, J. F. *Nano Lett.* **2003,** 3, 373-378.

[83] Zheng, H. *Science* **2009,** 324, 1309-1312.

[84] Evans, J. E.; Jungjohann, K. L.; Browning, N. D.; Arslan, I. *Nano Lett.* **2011,** 11, 2809-2813.

[85] Chai, J.; Liao, X.; Giam, L. R.; Mirkin, C. A. *J. Am. Chem. Soc.* **2012,** 134, 158-161.

[86] Yuk, J. M. *Science* **2012,** 336, 61-64.

[87] Liao, H. G.; Cui, L.; Whitelam, S.; Zheng, H. *Science* **2012,** 336, 1011-1014.

[88] Wang, C.; Qiao, Q.; Shokuhfar, T.; Klie, R. F. *Adv. Mater.* **2014,** 26, 3410-3414.

[89] Li, Z. Y. *Nature* **2008,** 451, 46-49.

[90] Scott, M. C. *Nature* **2012,** 483, 444-448.

[91] Aert, S. V.; Batenburg, K. J.; Rossell, M. D.; Erni, R.; Tendeloo, G. V. *Nature* **2011,** 470, 374-377.

[92] Park, J. *Science* **2015,** 349, 290-295.

[93] Chen, C. C. *Nature* **2013,** 496, 74-77.

[94] Rieger, J. *Faraday Discuss.* **2007,** 136, 265-277.

[95] Pouget, E. M. *J. Am. Chem. Soc.* **2010,** 132, 11560-11565.

[96] Davis, T. M. *Nat. Mater.* **2006,** 5, 400-408.

[97] Cölfen, H.; Antonietti, M., *Mesocrystals and Nonclassical Crystallization*. Wiley: 2008.

[98] Shields, S. P.; Richards, V. N.; Buhro, W. E. *Chem. Mater.* **2010,** 22, 3212-3225.

[99] Banfield, J. F.; Welch, S. A.; Zhang, H.; Ebert, T. T.; Penn, R. L. *Science* **2000,** 289, 751-754.

[100] Penn, R. L.; Banfield, J. F. *Science* **1998,** 281, 969-971.

[101] Penn, R. L.; Banfield, J. F. *Am. Miner.* **1998,** 83, 1077-1082.

[102] Penn, R. L.; Banfield, J. F. *Geochim. Cosmochim. Acta* **1999,** 63, 1549-1557.

[103] Li, D. *Science* **2012,** 336, 1014-1018.

[104] Pacholski, C.; Kornowski, A.; Weller, H. *Angew. Chem. Int. Ed. Engl.* **2002,** 41, 1188-1191.

[105] Tang, Z.; Kotov, N. A.; Giersig, M. *Science* **2002,** 297, 237-240.

[106] Yu, J. H. *J. Am. Chem. Soc.* **2005,** 127, 5662-5670.

[107] Yuwono, V. M.; Burrows, N. D.; Soltis, J. A.; Penn, R. L. *J. Am. Chem. Soc.* **2010,** 132, 2163-2165.

[108] Shanbhag, S.; Kotov, N. A. *J. Phys. Chem. B* **2006,** 110, 12211-12217.

[109] Huis, M. A. v. *Nano Lett.* **2008,** 8, 3959-3963.

[110] Min, Y.; Akbulut, M.; Kristiansen, K.; Golan, Y.; Israelachvili, J. *Nat. Mater.* **2008,** 7, 527-538.

[111] Bishop, K. J. M.; Wilmer, C. E.; Soh, S.; Grzybowski, B. A.

*Small* **2009,** 5, 1600-1630.

[112] Batista, C. A. S.; Larson, R. G.; Kotov, N. A. *Science* **2015,** 350, 1242477.

[113] Nie, Z. *Nat. Mater.* **2007,** 6, 609-614.

[114] Li, M.; Schnablegger, H.; Mann, S. *Nature* **1999,** 402, 393-395.

[115] Talapin, D. V. *Nature* **2009,** 461, 964-967.

[116] Keys, A. S.; Glotzer, S. C. *Phys. Rev. Lett.* **2007,** 99, 235503.

[117] Tang, Z.; Zhang, Z.; Wang, Y.; Glotzer, S. C.; Kotov, N. A. *Science* **2006,** 314, 274-278.

[118] Zhang, Z.; Tang, Z.; Kotov, N. A.; Glotzer, S. C. *Nano Lett.* **2007,** 7, 1670-1675.

[119] Schliehe, C. *Science* **2010,** 329, 550-553.

[120] Zherebetskyy, D. *Science* **2014,** 344, 1380-1384.

[121] Joo, J.; Son, J. S.; Kwon, S. G.; Yu, J. H.; Hyeon, T. *J. Am. Chem. Soc.* **2006,** 128, 5632-5633.

[122] Yu, J. H. *Nat. Mater.* **2010,** 9, 47-53.

[123] Son, J. S. *Angew. Chem. Int. Ed. Engl.* **2009,** 48, 6861-6864.

[124] Son, J. S. *Small* **2012,** 8, 2394-2402.

[125] Son, J. S. *Adv. Mater.* **2011,** 23, 3214-3219.

[126] Yang, J.; Son, J. S.; Yu, J. H.; Joo, J.; Hyeon, T. *Chem. Mater.* **2013,** 25, 1190-1198.

[127] Liu, Y. H.; Wang, F.; Wang, Y.; Gibbons, P. C.; Buhro, W. E. *J. Am. Chem. Soc.* **2011,** 133, 17005-17013.

[128] Wang, F. *Acc. Chem. Res.* **2015,** 48, 13-21.

[129] Lhuillier, E. *Acc. Chem. Res.* **2015,** 48, 22-30.

[130] Ithurria, S.; Bousquet, G.; Dubertret, B. *J. Am. Chem. Soc.* **2011,** 133, 3070-3077.

[131] Li, Z.; Peng, X. *J. Am. Chem. Soc.* **2011,** 133, 6578-6586.

[132] Chen, D.; Gao, Y.; Chen, Y.; Ren, Y.; Peng, X. *Nano Lett.* **2015,** 15, 4477-4482.

[133] Herrmann, G.; Gleiter, H.; Bäro, G. *Acta Metall.* **1976,** 24, 353-359.

[134] Ouyang, G.; Wang, C. X.; Yang, G. W. *Chem. Rev.* **2009,** 109, 4221-4247.

[135] Boneschanscher, M. P. *Science* **2014,** 344, 1377-1380.

[136] Sandeep, C. S. S. *Acs Nano* **2014,** 8, 11499-11511.

[137] Liao, H. G. *Science* **2014,** 345, 916-919.

[138] Bergström, L.; Sturm, E. V.; Salazar-Alvarez, G.; Cölfen, H. *Acc. Chem. Res.* **2015,** 48, 1391-1402.

[139] Zhou, L.; O'Brien, P. *J. Phys. Chem. Lett.* **2012,** 3, 620-628.

[140] Schwahn, D.; Ma, Y.; Cölfen, H. *J. Phys. Chem. C* **2007,** 111, 3224-3227.

[141] Cölfen, H.; Mann, S. *Angew. Chem. Int. Ed. Engl.* **2003,** 42, 2350-2365.

[142] Wang, Y.; He, J.; Liu, C.; Chong, W. H.; Chen, H. *Angew.*

*Chem. Int. Ed. Engl.* **2015,** 54, 2022-2051.

[143] Gu, J.; Zhang, Y. W.; Tao, F. *Chem. Soc. Rev.* **2012,** 41, 8050-8065.

[144] Fletcher, N. H. *J. Chem. Phys.* **1958,** 29, 572-576.

[145] Zhong, X.; Xie, R.; Zhang, Y.; Basché, T.; Knoll, W. *Chem. Mater.* **2005,** 17, 4038-4042.

[146] Kwon, S. G. *Nat. Mater.* **2015,** 14, 215-223.

[147] Winkler, P. M. *Science* **2008,** 319, 1374-1377.

[148] Pruppacher, H. R.; Klett, J. D., 1997.

[149] Reiss, P.; Protière, M.; Li, L. *Small* **2009,** 5, 154-168.

[150] Ithurria, S.; Guyot-Sionnest, P.; Mahler, B.; Dubertret, B. *Phys. Rev. Lett.* **2007,** 99, 265501.

[151] Jesser, W. A.; Kuhlmann-Wilsdorf, D. *Phys. Stat. Sol.* **1967,** 19, 95-105.

[152] Matthews, J. W.; Blakeslee, A. E. *J. Cryst.Growth* **1974,** 27,

118-125.

[153] Smith, A. M.; Mohs, A. M.; Nie, S. *Nat. Nanotechnol.* **2009,** 4, 56-63.

[154] Moseley, P.; Curtin, W. A. *Nano Lett.* **2015,** 15, 4089-4095.

[155] Kwon, K. W.; Shim, M. *J. Am. Chem. Soc.* **2005,** 127, 10269-10275.

[156] Buck, M. R.; Bondi, J. F.; Schaak, R. E. *Nat. Chem.* **2012,** 4, 37-44.

[157] Grünwald, M.; Lutker, K.; Alivisatos, A. P.; Rabani, E.; Geissler, P. L. *Nano Lett.* **2013,** 13, 1367-1372.

[158] Tolbert, S. H.; Alivisatos, A. P. *J. Chem. Phys.* **1995,** 102, 4642-4656.

[159] Strasser, P. *Nat. Chem.* **2010,** 2, 454-460.

[160] Zhang, S. *J. Am. Chem. Soc.* **2014,** 136, 7734-7739.

[161] Brokman, A.; Balluffi, R. W. *Acta Mater.* **1981,** 29, 1703-1719.

[162] Trampert, A.; Ploog, K. H. *Cryst. Res. Technol.* **2000,** 35, 793-806.

[163] Buonsanti, R. *J. Am. Chem. Soc.* **2006,** 128, 16953-16970.

[164] Mokari, T.; Rothenberg, E.; Popov, I.; Costi, R.; Banin, U. *Science* **2004,** 304, 1787-1790.

[165] Mokari, T.; Sztrum, C. G.; Salant, A.; Rabani, E.; Banin, U. *Nat. Mater.* **2005,** 4, 855-863.

[166] Zhang, J.; Tang, Y.; Lee, K.; Ouyang, M. *Science* **2010,** 327, 1634-1638.

[167] Gu, H.; Zheng, R.; Zhang, X.; Xu, B. *J. Am. Chem. Soc.* **2004,** 126, 5664-5665.

[168] Wu, H. *J. Am. Chem. Soc.* **2011,** 133, 14327-14337.

# Chapter 2. Size Dependence of Metal–Insulator Transition in Stoichiometric $Fe_3O_4$ Nanocrystals

## 2.1 Introduction

Among various metal oxide materials, $Fe_3O_4$, the oldest known magnetic material, is one of the most actively studied materials with a curie temperature of 858 K. In 1939, Verwey reported that bulk $Fe_3O_4$, which is fairly conductive with a half-metallic character at room temperature, becomes electrically insulating below 123 K, which is now called the Verwey transition temperature ($T_V$) [1]. Recently, it was reported that below the Verwey transition $Fe^{2+}$ and $Fe^{3+}$ in octahedral sites form a very unusual three-Fe-site "trimerons" ground state [2-4]. Meanwhile, over the last two decades, iron oxide (magnetite ($Fe_3O_4$) and maghemite ($\gamma$-$Fe_2O_3$)) nanocrystals (NCs) have been intensively investigated for their various biomedical applications including magnetic resonance imaging (MRI) contrast agents, magnetic biosensors, and heating mediators for magnetic fluid hyperthermia [5-11]. Especially, a recent development in synthesis of uniform and size-

controllable NCs [12-14] has enabled the size-dependent physical property characterization and their applications [15-24]. Despite the tremendous progresses in $Fe_3O_4$ NCs [15, 25-30], it is still an open question how the Verwey transition changes as the particle size gets reduced and in particular on the region of nanometer scale. The most critical difficulty in this size-dependent characterization of the Verwey transition is the synthesis of uniform and stoichiometric $Fe_3O_4$ NCs [16] because the Verwey transition is reported to be extremely sensitive to oxygen stoichiometry [31]. Most previous studies on the Verwey transition of $Fe_3O_4$ NCs suffer from the difficult problem of oxygen off-stoichiometry, which is an all pervasive issue of every oxide materials including high-temperature superconductors [32] and, more recently, resistive random-access memory (R-RAM) [33] and multiferroics [34] to name only a few.

## 2.2 Experimental Section

We synthesized stoichiometric and uniform-sized $Fe_3O_4$ NCs whose diameters ranged from 5 to 100 nm using thermal decomposition of iron acetylacetonate ($Fe(acac)_3$) precursor in the presence of oleic acid surfactant [12]. We could synthesize $Fe_3O_4$ NCs with sizes ranging from 5 to 89 nm by varying the precursor-to-surfactant ratios (one-pot thermal-decomposition method).

Materials.

Iron(III) acetylacetonate (99+%) was purchased from Acros organics. Oleic acid (technical grade, 90%) and benzyl ether (98%) were purchased from Sigma-Aldrich. These chemicals are used without further purification.

Synthesis.

We synthesized stoichiometric and uniform-sized $Fe_3O_4$ NCs whose diameters ranged from 5 to 100 nm. Magnetite NCs were synthesized by decomposing $Fe(acac)_3$ thermally in benzyl ether and

oleic acid. We modified the previous synthetic methods to control the nanocrystal sizes and stoichiometry [12, 35, 36]. The particle sizes could be tuned by two different methods. The first is the one-pot thermal-decomposition method and the other is the seed-mediated growth method. We synthesized NCs under the reductive gas mixture of $CO/CO_2$ 4/96 (in mass ratio). This reductive carbon monoxide gas enables us to control the oxidation state of magnetite [37, 38]. In practice, NCs synthesized under the inert gas (Ar gas) atmosphere show a suppression of $T_V$, which is caused by off-stoichiometry of magnetite NCs. The one-pot thermal-decomposition procedure to synthesize 36 nm-sized magnetite NCs is as follows. 21.3 g (60 mmol) of iron(III) acetylacetonate and 33.9 g (120 mmol) of oleic acid were dissolved in 312.0 g (300 ml) of benzyl ether. The mixture was degassed for 1 hr at room temperature. Rigorous magnetic stirring is necessary during the entire reaction. The mixture was heated up to 290 $^oC$ under $CO/CO_2$ 4/96 (in mass ratio) gas bubble [39]. The mixture was refluxed at 290 $^oC$ for 30 min and cooled down. After cooling at room temperature, we centrifuged the mixture at 8000 rpm for 10 min to precipitate $Fe_3O_4$ NCs. Afterwards, the precipitate was washed several times using toluene and ethanol as solvent and non-solvent, respectively. The as-

synthesized NCs were then stored under inert gas to avoid oxidation after the synthesis. The sizes of the $Fe_3O_4$ NCs could be controlled by varying the experimental conditions. For example, when the amount of iron(III) acetylacetonate was changed to 6.09 g, while keeping all the other reaction conditions unchanged, 5 nm-sized NCs were obtained.

During the whole procedure of the synthesis, separation, and measurement, NCs were rigorously isolated from oxygen source. After synthesis under $CO/CO_2$ atmosphere, NCs were washed and dried in Ar filled glovebox to obtain powder form. The powder of NCs was sealed in a gelatin capsule in the glovebox and transferred to the chamber of MPMS to measure magnetization under high vacuum. While transferring, the capsule containing NC powder was sealed in a secondary container filled with Ar in order to avoid air contact.

Characterization of $Fe_3O_4$ nanocrystals.

We stored and characterized the NCs in either inert atmosphere or high vacuum throughout the experiments so that the chance for oxidation after synthesis was minimal.

TEM.

JEOL JEM-3010 electron microscope with 300 kV was used to take the TEM images. The sample grid was prepared by sonicating the NCs dispersion in toluene and by dropping onto an ultrathin carbon film coated with copper grid.

X-ray diffraction.

Synchrotron high resolution powder diffraction (HRPD) measurements were performed at the 9B beam line of Pohang Accelerator Laboratory (PAL, Pohang, Republic of Korea). The incident X-ray source was vertically collimated by mirror and monochromatized to $\lambda$= 1.5472 Å by a double-crystal Si(111) monochromator (DCM). The Rietveld refinement was performed by using FullProf software (http://www.ill.eu/sites/fullprof) [40]. We used Thompson-Cox-Hastings (TCH) pseudo-Voigt profile function to fit the HRPD pattern [41]. We also carried out a temperature-dependence study of the XRD (cryo-XRD) pattern using a Bruker D8 Discover system with Oxford cryosystems. Sample is exposed to air for few minutes when mounting for measuring the XRD data.

Magnetic property characterization.

Magnetization measurements were performed from 5 to 300 K under magnetic field of 10 mT by a Quantum Design SQUID magnetometer MPMS 5XL.

Heat capacity measurement.

Heat capacity measurements were performed by a Quantum Design PPMS-14 from 5 to 150 K. Sample is exposed to air for few minutes when mounting for measuring the heat capacity ($C_P$) data.

Conductance measurement.

The as-synthesized magnetite NCs are insulating because of insulating organic surfactant (oleic acid) on the surface of NCs. To remove the insulating surfactant layer, the as-synthesized NCs were treated with hydrazine before measuring conductance [42]. After being washed, the as-synthesized NCs were dispersed and sonicated in 1 M hydrazine ($N_2H_2$) in THF ($C_4H_8O$) solution (Sigma-Aldrich #433632)

in Ar atmosphere to remove the surfactant (organic layer). This procedure reduces contact resistance between NCs significantly. After 3 min of dispersion, the insulating organic layer of NCs was effectively removed without changing $T_V$ (Figure 2.1). After the hydrazine treatment, NCs were washed again and dried in vacuum for 2 hr before pressed into pellet in Ar-filled glove box. Two copper wires were attached on the same side of the sample using silver epoxy (2-probe geometry). Sample is exposed to air for few minutes when mounting for measuring the conductance (G) data. The conductance of magnetite NC pellet was increased by about 6 orders of magnitude in comparison to the sample without the hydrazine treatment. Home-built transport measurement set-up including a Keithley 6430 sub-femtoamp remote sourcemeter and a Lake Shore 331 temperature controller was used to measure conductance. In every measurement, the current was fixed and the bias direction was altered at each step and averaged to avoid electronic offsets.

X-ray absorption spectroscopy (XAS).

The XANES and EXAFS measurements were conducted at the

10C beam line at Pohang Accelerator Laboratory (PAL). The incident X-ray beam was monochromatized by using a liquid-$N_2$ cooled Si(111) double crystal monochromator (DCM). The data were taken on a transmission mode. Ionization chambers were used to quantify the incident and transmitted beams. The spectra were normalized by Athena program.

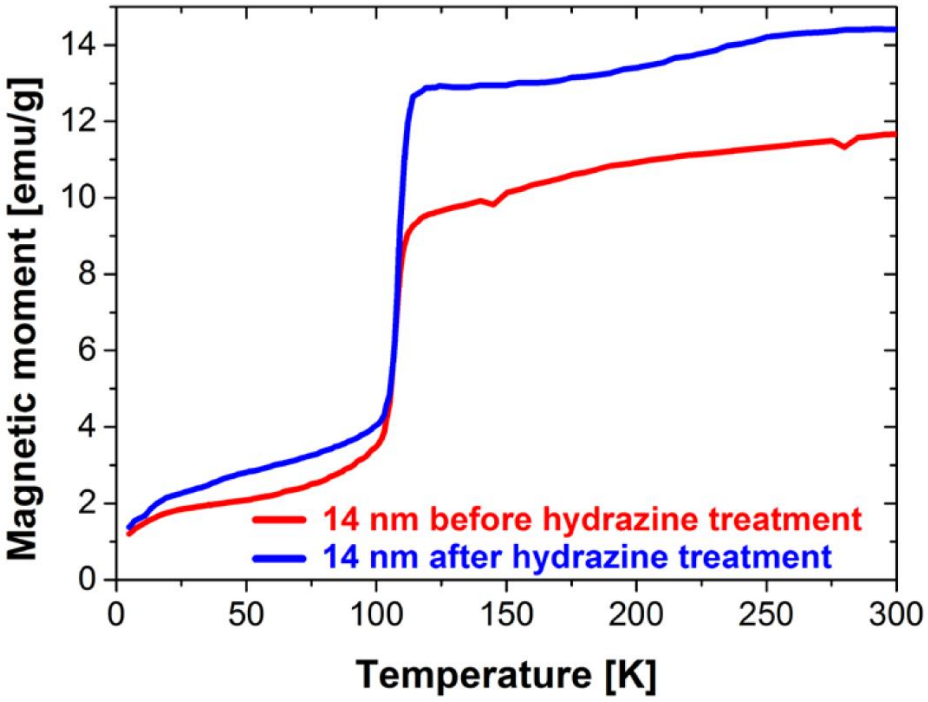


**Figure 2.1** Zero-field-cooled (ZFC) magnetization data measured with magnetic field of 10 mT for 14 nm NCs. The red line denotes the as-synthesized NCs and the blue line denotes NCs after the hydrazine treatment. NCs after the hydrazine treatment show a big increase in magnetic moment owing to the reduced mass ratio of non-magnetic surfactant. $T_V$ represented by stepwise magnetic moment change near 120 K shows no visible difference between the two.

## 2.3 Synthesis of uniform sized $Fe_3O_4$ nanocrystals

The particle sizes were determined by using transmission electron microscopy (TEM) (Figure 2.2). TEM images and histograms of NCs show that the particle size distributions are narrow ($\sigma < 15\%$). The high-resolution TEM (HRTEM) images and the selective-area electron diffraction (SAED) patterns (Figure 2.3) show a highly crystalline structure of the $Fe_3O_4$ NCs. The oxidation state of Fe can be qualitatively examined by Fe K-edge X-ray absorption near edge structure (XANES) spectra (Figure 2.4) [13]. We measured XANES of NCs and compared with iron oxide standards, that is, maghemite ($\gamma$-$Fe_2O_3$) and magnetite ($Fe_3O_4$). $\gamma$-$Fe_2O_3$ and $Fe_3O_4$ have different features near the edge as shown in Figure 2.4. We confirm that the Fe K-edge peak of NCs are close to $Fe_3O_4$ standard.

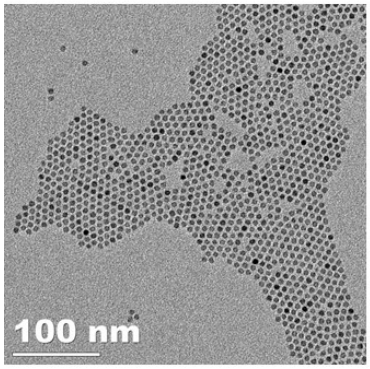
100 nm

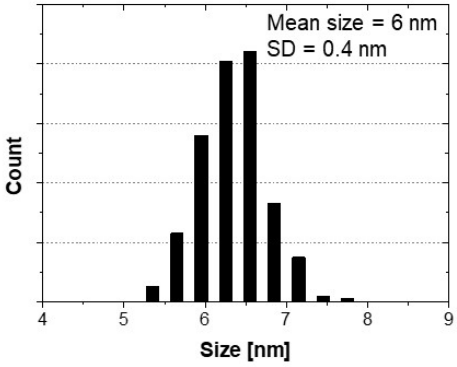
Mean size = 6 nm
SD = 0.4 nm
Count
4
5
6
7
8
9
Size [nm]

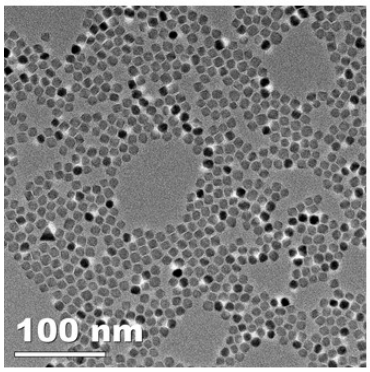
100 nm

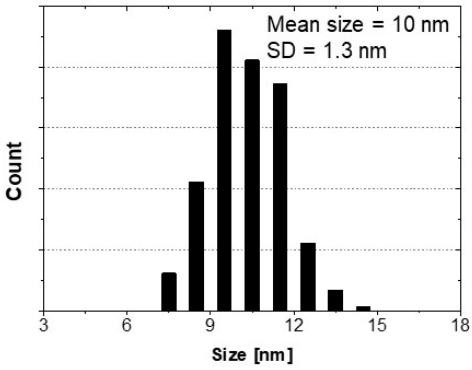
Mean size = 10 nm
SD = 1.3 nm
Count
3
6
9
12
15
18
Size [nm]

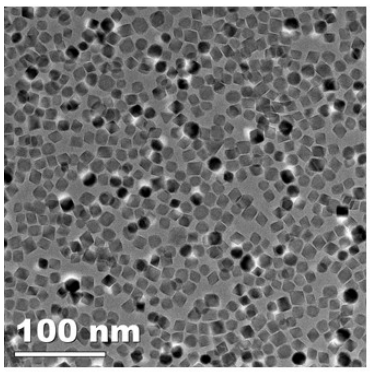
100 nm

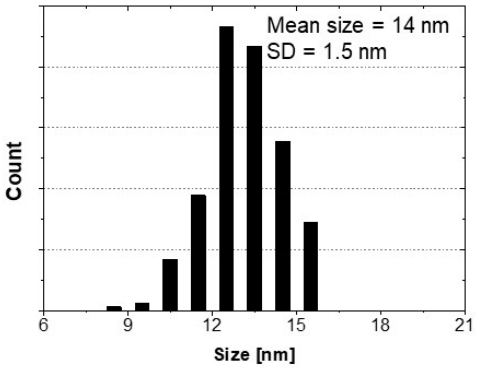
Mean size = 14 nm
SD = 1.5 nm
Count
6
9
12
15
18
21
Size [nm]

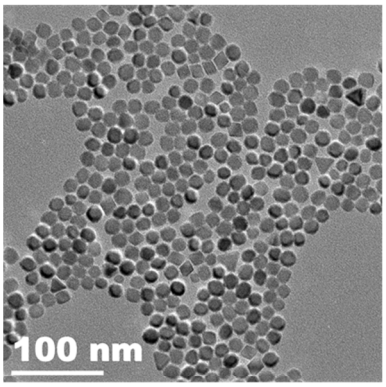
100 nm

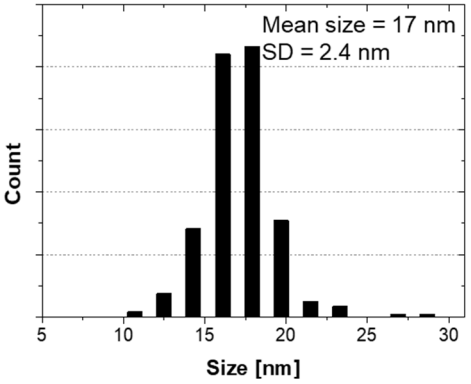
Mean size = 17 nm
SD = 2.4 nm
Count
5
10
15
20
25
30
Size [nm]

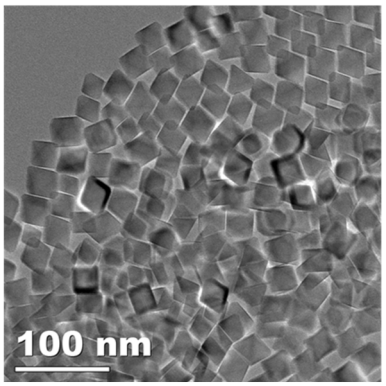
100 nm

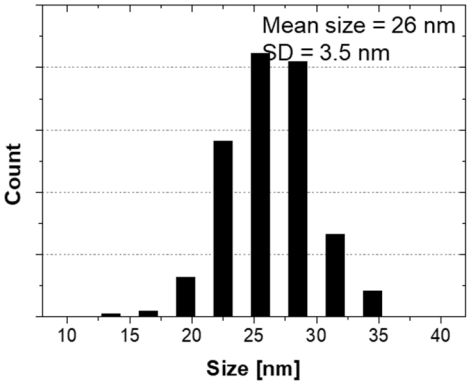
Mean size = 26 nm
SD = 3.5 nm
Count
10
15
20
25
30
35
40
Size [nm]

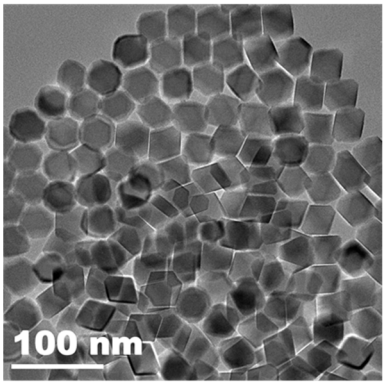
100 nm

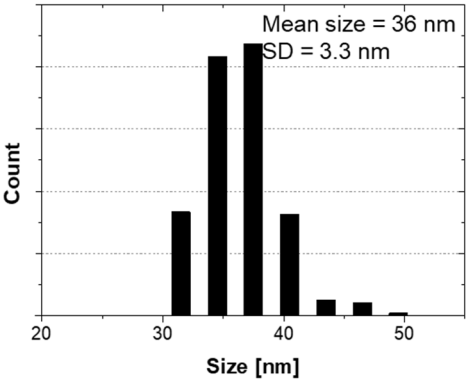
Mean size = 36 nm
SD = 3.3 nm
Count
20
30
40
50
Size [nm]

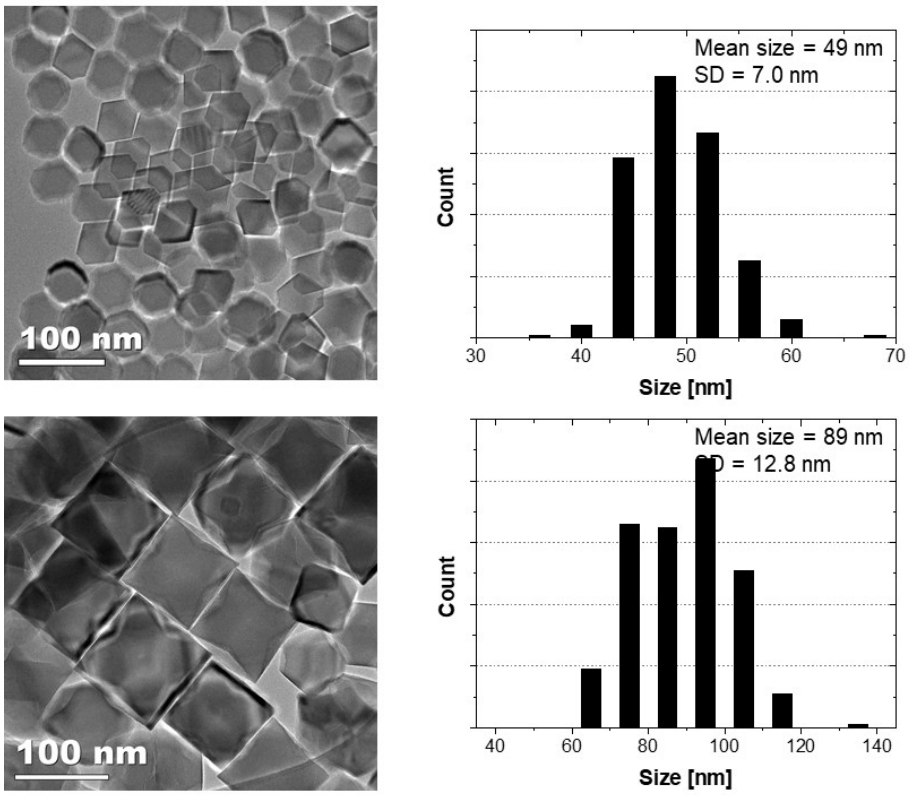


**Figure 2.2** TEM images and size distribution histograms of one-pot synthesized $Fe_3O_4$ NCs.

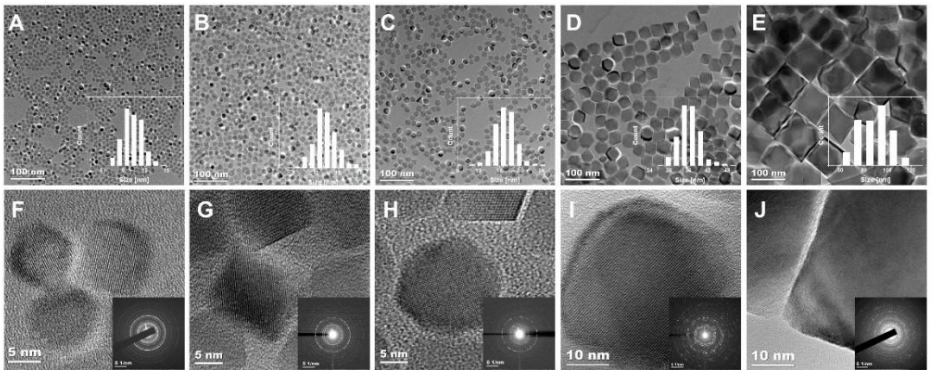


**Figure 2.3** TEM images (A–E) and HRTEM images (F–J) of $Fe_3O_4$ NCs. Particle size distribution histograms are shown in the inset of (A–E) with SAED patterns in the inset of (F–J): (A,F) 10 nm, (B,G) 14 nm, (C,H), 17 nm, (D,I) 36 nm, and (E,J) 89 nm. The histograms show narrow particle size distributions while the HRTEM images with SAED patterns attest to the high crystallinity.

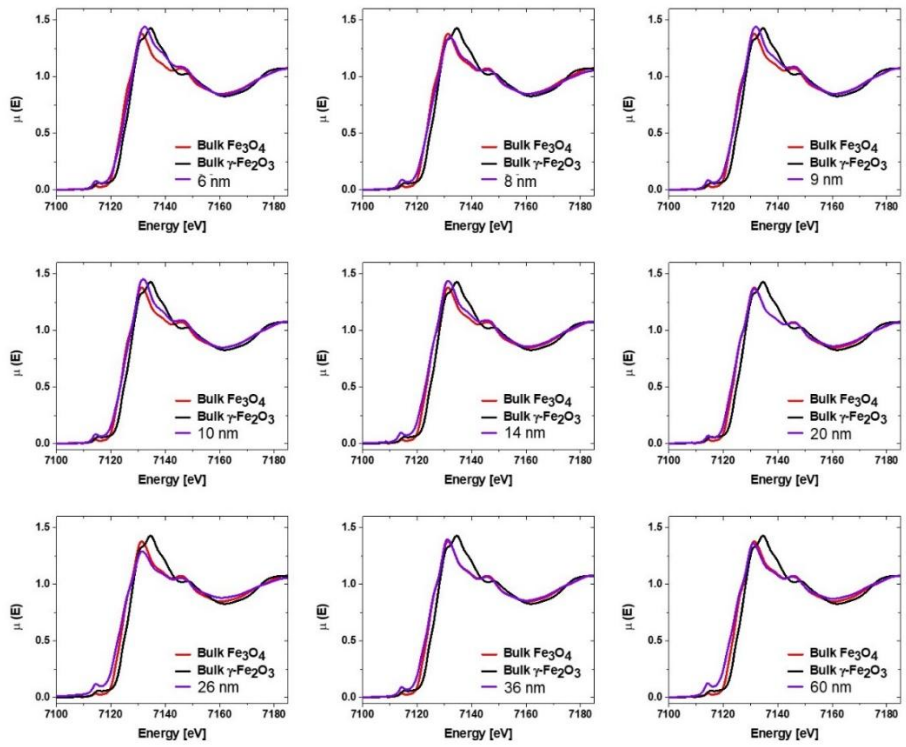


**Figure 2.4** Fe K-edge XANES spectra of various-sized $Fe_3O_4$ NCs and bulk $\gamma$-$Fe_2O_3$ and $Fe_3O_4$ standard samples. The dotted line indicated the white line peak position of bulk $Fe_3O_4$. It is clear that all the NCs are magnetite ($Fe_3O_4$), not maghemite ($\gamma$-$Fe_2O_3$).

The HRPD patterns (Figure 2.5) show that the peak positions of the $Fe_3O_4$ NCs are consistent with those of bulk $Fe_3O_4$ (blue bars, JCPDS file, No. 19-0629) that carries no sign of other impurities, such as wüstite (FeO) [16]. The size and stoichiometry of NCs were estimated by the Rietveld refinement using the Fullprof software [40]. The crystal sizes estimated by Rietveld refinement are found to be comparable to the particle sizes measured by TEM (Table 2.1). Off-stoichiometry parameters (δ), which is defined as $Fe_{3(1-\delta)}O_4$, of the NCs are shown in (Table 2.2). The data show that the NCs are stoichiometric $Fe_3O_4$ within error range of 6.5% at maximum. Also, the value of δ does not show any size dependence, which proves that the oxidation state of Fe is not affected by the surface-to-volume ratio.

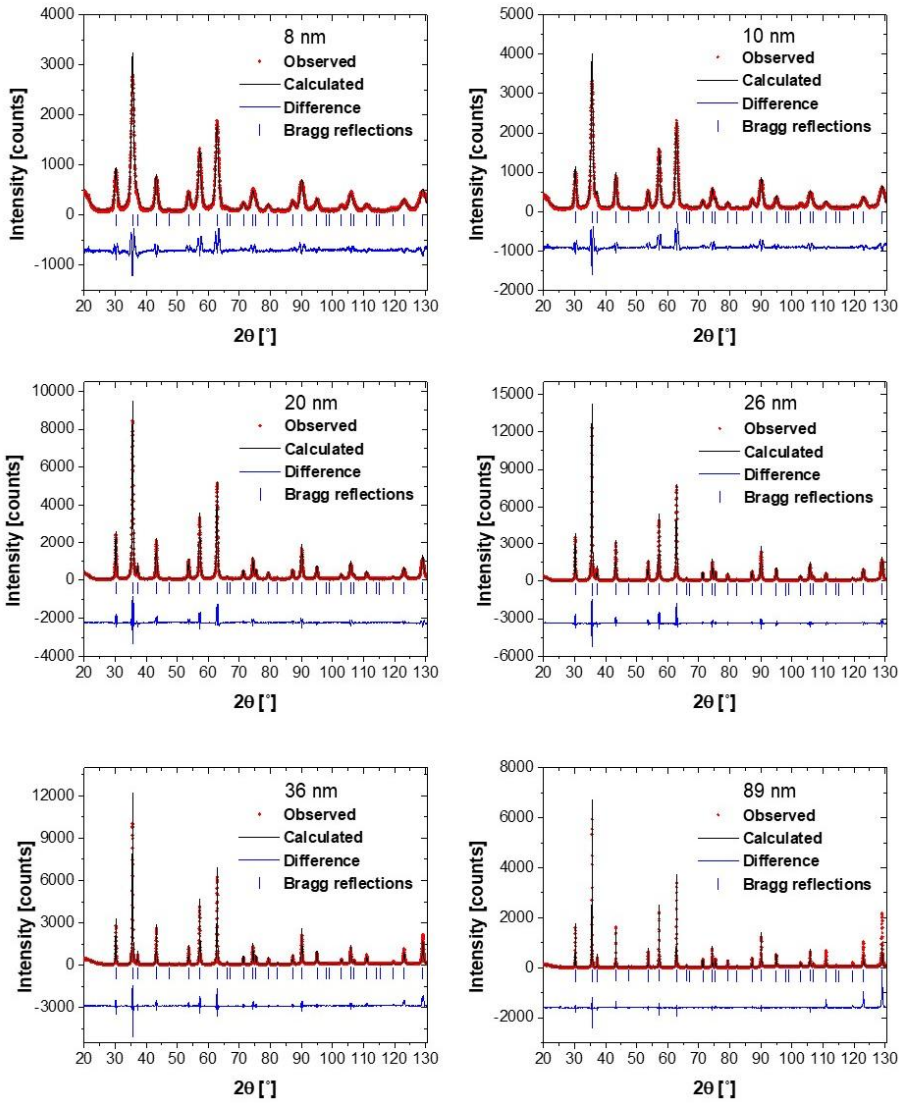


**Figure 2.5** HRPD patterns of $Fe_3O_4$ NCs at room temperature overlapped with profile functions of Rietveld refinement (black). The red dots are obtained from the experimentally observed patterns. The black lines are the refinement data obtained by the Thompson-Cox-

Hastings (TCH) pseudo-Voigt profile function [41]. The blue curves on the bottom of each graph are the difference between the observed patterns and the refinement data. The blue vertical bars indicate the Bragg peak positions (JCPDS file, No. 19-0629).

| Chemical formula | $Fe_3O_4$ | | | | | |
|---|---|---|---|---|---|---|
| Space group | $Fd\bar{3}m$ (#227) | | | | | |
| X-ray wavelength [Å] | 1.54720 | | | | | |
| 2θ scan range [°] | 10 – 130.5 | | | | | |
| 2θ scan step [°] | 0.02 | | | | | |
| Particle size [nm] | 8 | 10 | 20 | 26 | 36 | 89 |
| Lattice parameter [Å] | 8.39477 | 8.39276 | 8.39532 | 8.39678 | 8.39391 | 8.39545 |
| Cell volume [$Å^3$] | 591.59 | 591.173 | 591.714 | 592.022 | 591.417 | 591.742 |
| $R_B$ [%] | 7.36 | 9.51 | 6.60 | 6.16 | 9.65 | 19.5 |
| $R_F$ [%] | 4.56 | 7.53 | 4.78 | 5.41 | 7.52 | 10.6 |
| $\chi^2$ | 5.85 | 7.53 | 7.01 | 8.78 | 8.12 | 3.90 |
| Crystal size [nm] | 7.2 | 9.8 | 19.0 | 27.8 | 32.9 | 61.7 |

**Table 2.1** Refined result of HRPD for NCs at 300 K with ideal stoichiometry model (Fe:O = 3:4).

| size [nm] | $R_B$ [%] | $R_F$ [%] | $\chi^2$ | $Fe_{3(1-\delta)}O_4$ |
|---|---|---|---|---|
| 5 | 11.0 | 8.36 | 16.4 | $\delta \sim 0.018$ |
| 8 | 6.54 | 3.51 | 5.60 | $\delta \sim 0.058$ |
| 10 | 8.46 | 6.17 | 7.14 | $\delta \sim 0.065$ |
| 20 | 6.12 | 4.23 | 6.82 | $\delta \sim 0.030$ |
| 36 | 9.50 | 7.14 | 8.08 | $\delta \sim 0.016$ |
| 89 | 19.6 | 10.6 | 3.90 | $\delta \sim 0.004$ |

**Table 2.2** Off-stoichiometry parameter δ of the $Fe_3O_4$ NCs and corresponding reliable factors, $R_B$, $R_F$, and $\chi^2$ derived by Rietveld refinement of HRPD Data.

In order to prepare stoichiometric NCs, we adjusted the electrochemical equilibrium condition of the synthesis by using $CO/CO_2$ gas mixture (Figure 2.6) [38]. In general, there is an equilibrium between $Fe^{2+}$ and $Fe^{3+}$ in iron oxide solid that is often expressed in terms of oxygen fugacity $fo_2$ as follows [31].

$$4Fe_3O_4 + O_2 \rightleftarrows 6Fe_2O_3$$

If the reaction condition is reductive so that $fo_2$ is lower than the equilibrium value $f^{\oplus}_{O_2}$, some $Fe^{3+}$ is reduced to $Fe^{2+}$ to restore the equilibrium. In other words, the ratio of $Fe^{2+}$ and $Fe^{3+}$ can be adjusted by the electrochemical potential of oxygen that in turn is controlled by the ratio of CO and $CO_2$ in the reaction atmosphere. Because we used $Fe(acac)_3$ as the precursor of iron oxide NCs, there are only $Fe^{3+}$ ions in the solution at the start of the reaction and the exact amount of $Fe^{3+}$ should be reduced to $Fe^{2+}$ to yield stoichiometric $Fe_3O_4$ NCs. In practice, the sharp Verwey transition (Figure 2.7, Figure 2.8, Figure 2.9) is observed in 89 nm- and 36 nm-sized NCs. Because the Verwey transition is extremely sensitive to off-stoichiometry, this result confirms that the synthesis under 4/96 $CO/CO_2$ atmosphere ensures the exact ratio of $Fe^{3+}/Fe^{2+}$ and the formation of stoichiometric $Fe_3O_4$ NCs. It should be noted that the ratio of $Fe^{3+}/Fe^{2+}$ is determined by the

electrochemical equilibrium but not by the size of the NCs. Consequently, the NCs with various sizes synthesized under 4/96 $CO/CO_2$ atmosphere should have the same $Fe^{3+}/Fe^{2+}$ ratio and stoichiometry as 89 and 36 nm-sized NCs.

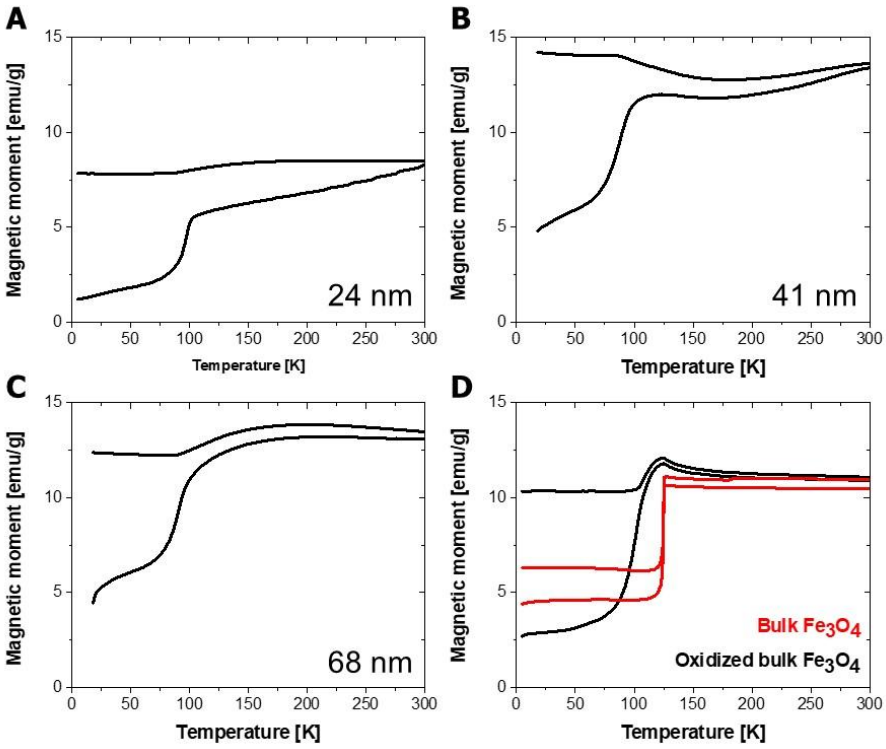


**Figure 2.6** Magnetization data measured with magnetic field of 10 mT for $Fe_3O_4$ NCs synthesized in Ar atmosphere. (A-C) ZFC, FC curves of NCs synthesized in the Ar atmosphere (synthesis scale of 2 mmol $Fe(acac)_3$). A magnetic moment slope near 100 K represents suppressed $T_V$. (D) Suppression of $T_V$ is also clear in oxidized bulk $Fe_3O_4$ (black line) compare to non-oxidized bulk $Fe_3O_4$ (red line). Bulk $Fe_3O_4$ powder was oxidized at 200 $^oC$ in air for 3 hr.

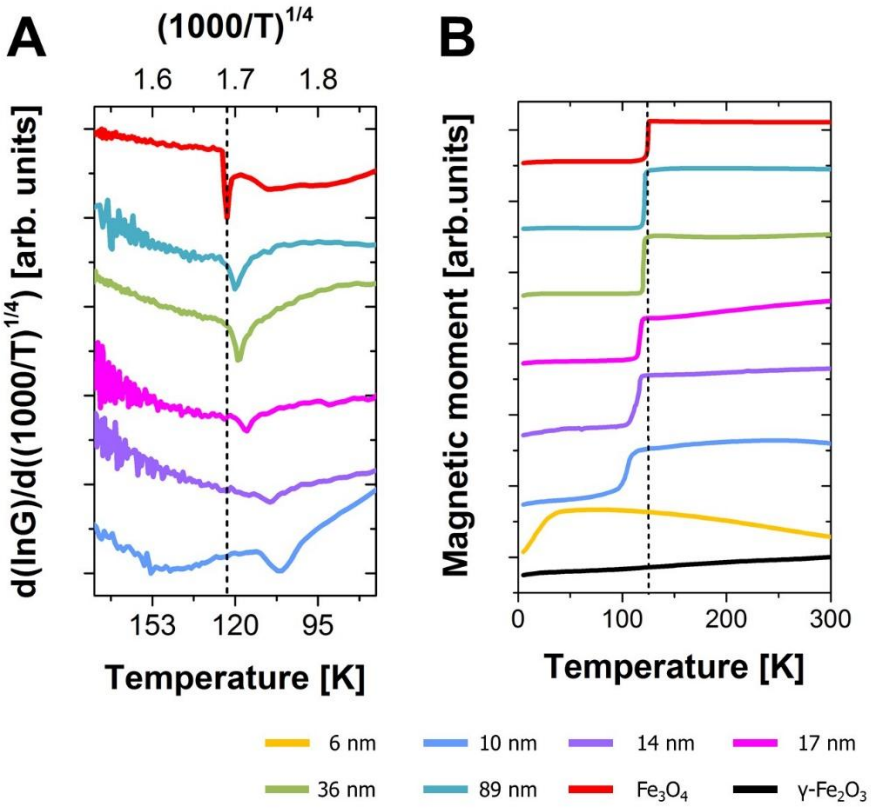


**Figure 2.7** Size-dependence of Metal-insulator transition. (A) Temperature dependence of first derivative of conductance (G). The sharp peaks correspond to the Verwey transition, still visible down to 10 nm although it shifts toward lower temperature with decreasing particle size. (B) ZFC magnetization data measured at magnetic field of 10 mT for various sized $Fe_3O_4$ NCs. The sharp drop in the magnetization near 120 K indicates the Verwey transition. The vertical dotted line indicates $T_V$ of bulk $Fe_3O_4$.

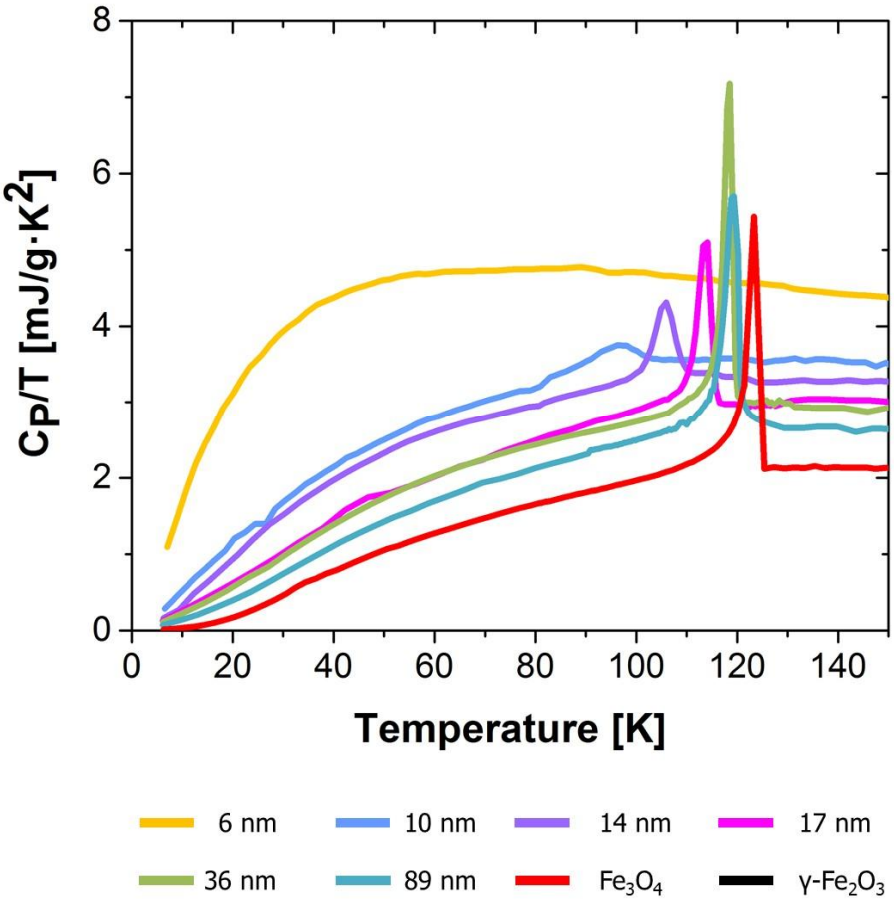


**Figure 2.8** The total heat capacity divided by temperature. As the particle size decreases, the sharp peak of the Verwey transition moves toward lower temperature and gets considerably weaker.

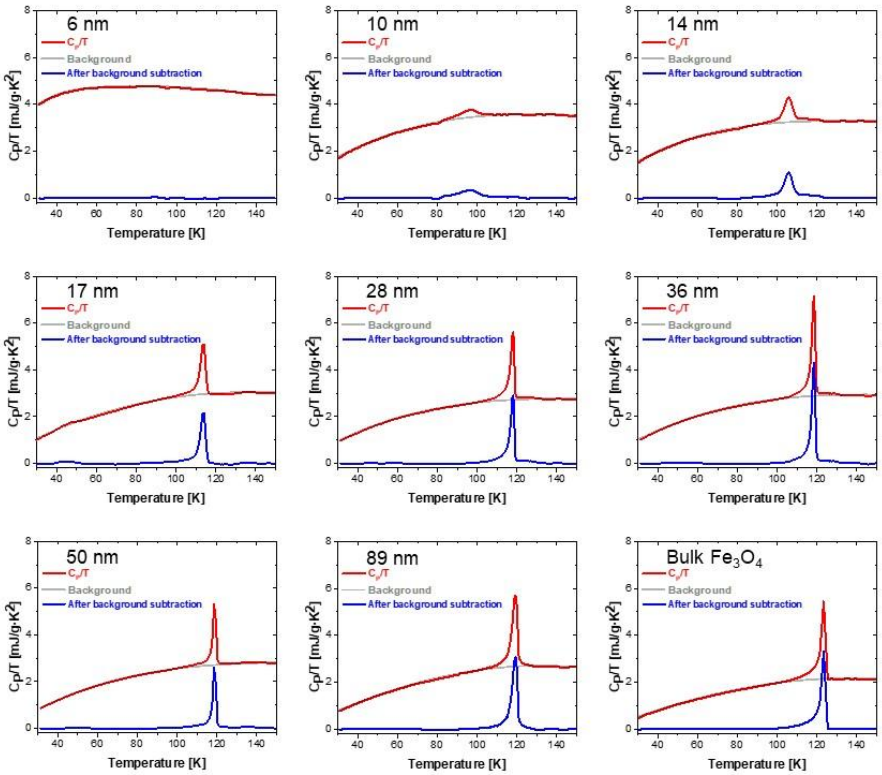


**Figure 2.9** Heat capacity (Red) and polynomial fitted background (Gray). The blue lines represent the heat capacity after background subtraction.

## 2.4 Metal-insulator transition of $Fe_3O_4$ nanocrystals

It is widely known that the Verwey transition of $Fe_3O_4$ is accompanied by various anomalies in the physical properties at $T_V$, [1, 2, 43] including magnetic moment (m), conductance (G), structural (space group) change, and heat capacity ($C_P$). First, we examined the structural change of NCs at the Verwey transition by using a cryo-XRD (Figure 2.10). For bulk $Fe_3O_4$, there is a drastic change in the crystal symmetry from monoclinic (Cc) below $T_V$ to inverse spinel cubic ($Fd\bar{3}m$) above $T_V$ [2]. For example, the (440) peak in the cubic phase is split into two peaks below $T_V$ with a reduction in the peak intensity in the low-temperature monoclinic phase [44, 45] as shown in the data for bulk $Fe_3O_4$, which is absent in $\gamma$-$Fe_2O_3$ (Figure 2.10). This change is still visible in NCs, for example, in 22 nm-sized NCs, and becomes considerably weaker as the particle size decreases.

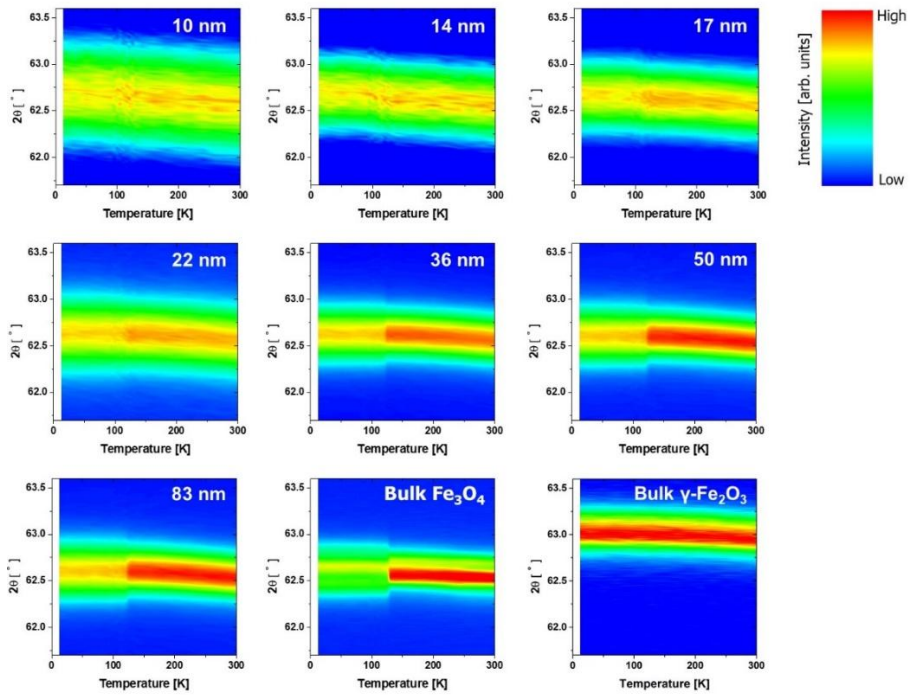


**Figure 2.10** Thermal evolution of (440) plane XRD peak based on the sizes of NCs. Peak broadenings and intensity reduction are clear below $T_V$. This is the evidence for the anticipated lattice distortion at the Verwey transition. Note that no sign is found to indicate such changes in the bulk $\gamma$-$Fe_2O_3$ data.

Furthermore, an abrupt change in the conductance is the clear evidence of the Verwey transition, that is, a metal–insulator transition (MIT). In the picture of charge ordering originally put forward by Verwey himself and further refined by more recent researches [2, 3], $Fe^{2+}$ and $Fe^{3+}$ are ordered into a unique linear three-Fe-site unit below $T_V$. These localized and charge-ordered electrons organize themselves making $Fe_3O_4$ electrically insulating below $T_V$. Above $T_V$, electrons are no more localized and can hop between $Fe^{2+}$ and $Fe^{3+}$ sites. In order to examine the size dependence of the MIT, we have measured the conductance of NCs to find that the sign of MIT gets progressively weaker as the particle size is reduced. In Figure 2.7A, the conductance (G) is plotted as $d(\ln G)/d(1000/T)^{1/4}$ versus $(1000/T)^{1/4}$; the minimum is clearly visible even in the data of 10 nm although the anomaly is much more suppressed and much broader than the minimum of bulk $Fe_3O_4$.

When $Fe_3O_4$ undergoes the MIT, there is also an anomaly in the magnetization data with a change in the magnetic easy axis; $Fe_3O_4$ is a spinel type ferrimagnetic material with $Fe^{3+}$ at the tetrahedral site (A) and $Fe^{2+}/Fe^{3+}$ at the octahedral site (B) having a strong antiferromagnetic interaction. For instance, bulk $Fe_3O_4$ shows a drastic

drop in the magnetization data at 123 K shown in Figure 2.7B, where we observed the MIT in the conductance measurement and the structure change, consistent with the reported results [43], which renders it another useful test of the Verwey transition in NCs. As clearly seen in our data, this anomaly in the magnetization moves only slightly toward lower temperatures and gets broader as the particle size decreases. Intriguingly, the Verwey transition disappears below 6 nm, where blocking temperature ($T_B$) becomes lower than $T_V$ (Figure 2.7B, Figure 2.11).

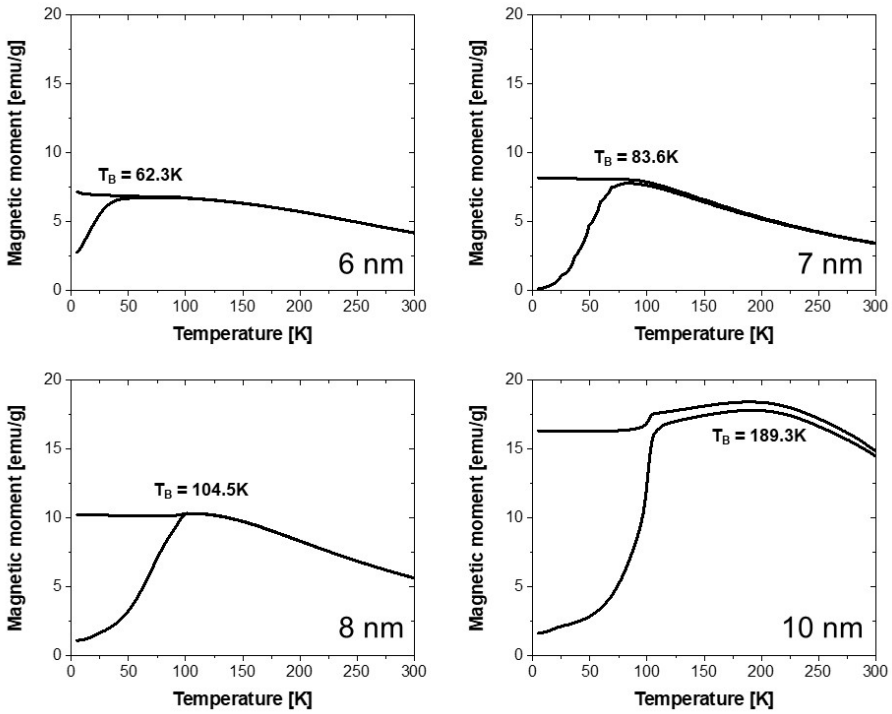


**Figure 2.11** ZFC, FC curves of small (< 10 nm) NCs at 10 mT. Below 8 nm, $T_B$ becomes lower than $T_V$ and the Verwey transition has disappeared.

Although the anomalies we observed in the cryo-XRD, conductance, and magnetization data are conspicuous, it is the heat capacity data that can confirm these anomalies as a truly thermodynamic transition as in the bulk $Fe_3O_4$. For example, it is possible that $T_V$ is masked by rapid decrease in the magnetic moment in the temperature range below blocking temperature ($T_B$). Thus, it is reassuring the heat capacity data measured on NCs shows a lambda-like anomaly just like that of bulk $Fe_3O_4$ (Figure 2.8). From this, we can deduce three statements. First and foremost, all the anomalies we observed in the NCs are a true Verwey transition on a nanometer scale, whose peak gets progressively broader while it moves toward lower-temperature. Second, the total area of the peak, corresponding to the total entropy of the Verwey transition for a given size of samples, shows a reduction as the particle size gets smaller although the transition temperature itself has barely changed, which indicates that lesser entropy is released for the Verwey transition of smaller NCs. Third, the peak of the Verwey transition is completely absent in the 6 nm-sized NCs (Figure 2.9), indicating that the Verwey transition disappears in $Fe_3O_4$ NCs smaller than 6 nm.

Thus, by combining our data in a wide-ranging size we can

confirm that the Verwey transition is size-independent down to 20 nm with a weak suppression of the transition temperature from 20 to 8 nm before suddenly disappearing below 6 nm (Figure 2.12). Interestingly, the size versus the Verwey transition temperature plot is well fitted with an exponential equation, $T_V = a \exp(-D/b) + T_o$ where a, b, and $T_o$ are fit parameters (Figure 2.13). The adjusted $R^2$ value of 0.937 from this fit is statistically meaningful and it is strongly suggested that there is quantitative relationship between the size of the NCs and $T_V$. There is a possibility that broken symmetry of the crystal structure and the presence of low-coordinated atoms at the surface of the NCs can affect the observed size-dependent behavior of the Verwey transition, which becomes more pronounced for the smaller NCs. Also, this result excludes the possibility of contribution from surface oxidation and disorder to the Verwey transition. If the stoichiometry of the NCs is changed by any effect from the surface, it is reasonable to expect that off-stoichiometry is proportional to the surface-to-volume ratio. That is, the off-stoichiometry parameter $\delta$ is proportional to 1/D where D is the size of the NC. Then, because the Verwey transition temperature $T_V$ is linearly dependent on $\delta$ [31], we should have $T_V \propto 1/D$, which is rejected by the exponential fit result in Figure 2.13.

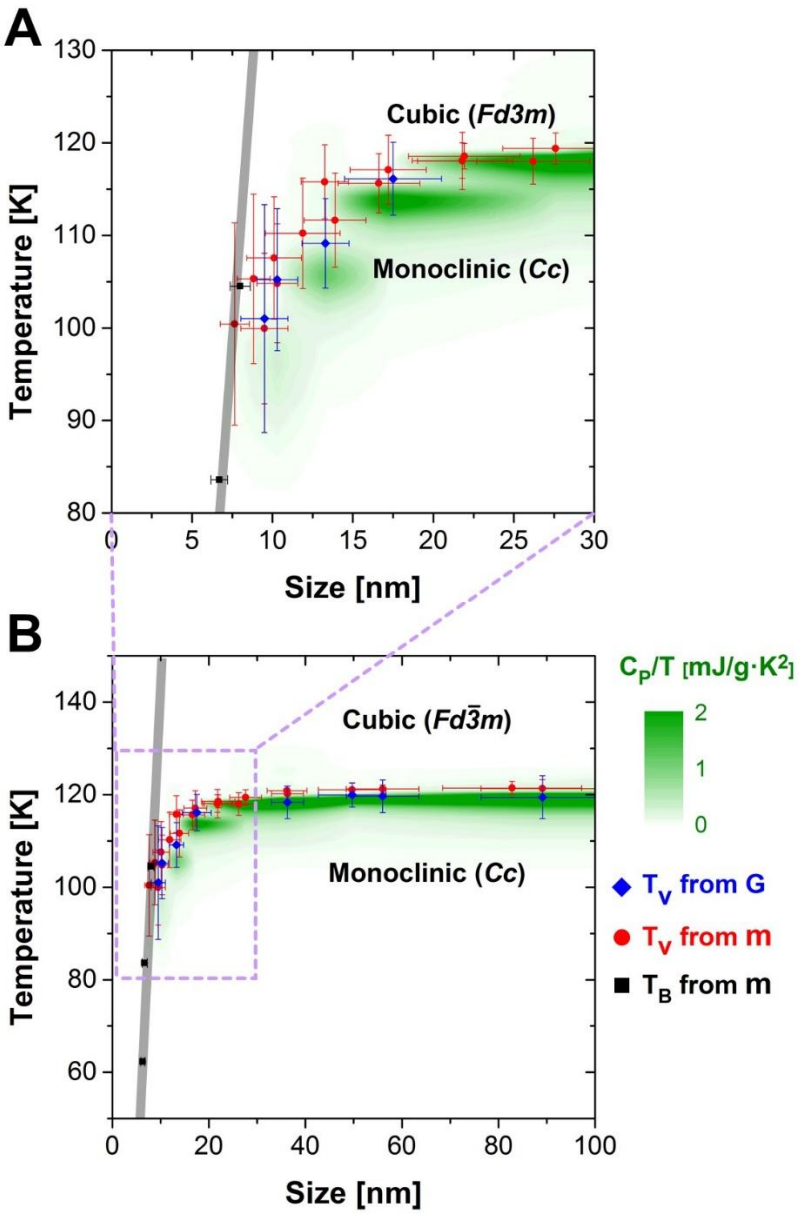


**Figure 2.12** Size dependence of $T_V$ for $Fe_3O_4$ NCs. The contour plot represents the heat capacity data after removing the contribution of

surfactant (see Figure 2.9). The symbols mark the Verwey transition temperature ($T_V$) determined from three different types of measurements: heat capacity (green, $C_P/T$), conductance (blue, G), and magnetic moment (red, m). The size dependence of blocking temperature ($T_B$) is also plotted from the same magnetization measurement (black). The gray line is a guide to the eye for the size dependence of $T_B$.

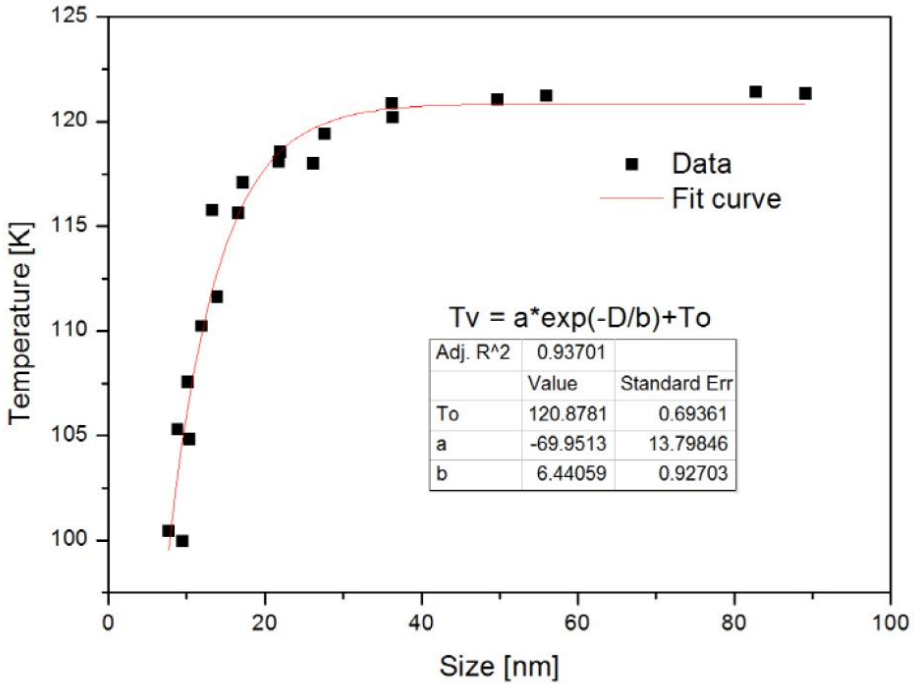


**Figure 2.13** Size dependence of $T_V$ for $Fe_3O_4$ NCs and the fit curve with the fit equation and the result. The data are re-plotted from Figure 2.12. In the fit equation, a, b, and $T_o$ are fit parameters and D is the size of the NCs.

## 2.5 Conclusions

This drastic size effect of the Verwey transition has never been reported before and reveals an unexpected yet intimate inner secret of this decades-old conundrum. As the history of seven decades-long researches shows, the origin of the Verwey transition is an extremely difficult problem and inevitably our ideas for this just uncovered experimental observation is bound to be speculative. Nevertheless, let us offer our thoughts that might well be found later useful for a full-fledge theoretical investigation. First, a commonly accepted explanation is that the spin degree of freedom is irrelevant for the Verwey transition unlike the other two degrees of freedom like charge and orbital. In this regards, it is interesting to note that the Verwey transition appears to suffer a drastic disappearance when the line of the transition temperature in Figure 2.12 hits a line of blocking temperature ($T_B$) (thick gray line in Figure 2.12), below which the giant magnetic moment of the single magnetic domain of the whole particle experiences a freezing of a thermally assisted over-the-barrier transition. Therefore, we propose with caution that after all the spin degree of freedom may not be that irrelevant for the Verwey transition. Second, we have demonstrated that the Verwey transition shows the remarkable

size effect that might as well prompt one to think of carrying out full unbiased first-principles calculations on $Fe_3O_4$ NCs with size just below and above the critical value of 6 nm. This new, nonetheless very challenging theoretical study will throw then the definite and ultimate light on our understanding of the seven decades long riddle.

In this work, we successfully synthesized uniform $Fe_3O_4$ NCs down to 5 nm, and undertook in-depth studies of the size-dependence of the Verwey transition. These comprehensive experimental investigations combined several microscopic and bulk characterization tools: X-ray absorption spectroscopy, conductance, X-ray diffraction, magnetization, and heat capacity. On the basis of these data, we conclude that there is a critical size for the Verwey transition at around 6 nm.

Most of the contents of this chapter were published in the article "Size Dependence of Metal–Insulator Transition in Stoichiometric $Fe_3O_4$ Nanocrystals" (*Nano Lett.* **2015**, 15, (7), 4337-4342).

## 2.6 References


[1] Verwey, E. J. *Nature* **1939,** 144, (3642), 327-328.

[2] Senn, M. S.; Wright, J. P.; Attfield, J. P. *Nature* **2012,** 481, (7380), 173-176.

[3] de Jong, S.; Kukreja, R.; Trabant, C.; Pontius, N.; Chang, C. F.; Kachel, T.; Beye, M.; Sorgenfrei, F.; Back, C. H.; Bräuer, B.; Schlotter, W. F.; Turner, J. J.; Krupin, O.; Doehler, M.; Zhu, D.; Hossain, M. A.; Scherz, A. O.; Fausti, D.; Novelli, F.; Esposito, M.; Lee, W. S.; Chuang, Y. D.; Lu, D. H.; Moore, R. G.; Yi, M.; Trigo, M.; Kirchmann, P.; Pathey, L.; Golden, M. S.; Buchholz, M.; Metcalf, P.; Parmigiani, F.; Wurth, W.; Föhlisch, A.; Schüßler-Langeheine, C.; Dürr, H. A. *Nature Mater.* **2013,** 12, (10), 882-886.

[4] Senn, M. S.; Loa, I.; Wright, J. P.; Attfield, J. P. *Phys. Rev. B* **2012,** 85, (12), 125119.

[5] Laurent, S.; Forge, D.; Port, M.; Roch, A.; Robic, C.; Vander Elst, L.; Muller, R. N. *Chem. Rev.* **2008,** 108, (6), 2064-2110.

[6] Xie, J.; Liu, G.; Eden, H. S.; Ai, H.; Chen, X. *Acc. Chem. Res.* **2011,** 44, (10), 883-892.

[7] Stanley, S. A.; Gagner, J. E.; Damanpour, S.; Yoshida, M.; Dordick, J. S.; Friedman, J. M. *Science* **2012,** 336, (6081), 604-608.

[8] Lee, N.; Hyeon, T. *Chem. Soc. Rev.* **2012,** 41, (7), 2575-2589.

[9] Lee, N.; Choi, Y.; Lee, Y.; Park, M.; Moon, W. K.; Choi, S. H.; Hyeon, T. *Nano Lett.* **2012,** 12, (6), 3127-3131.

[10] Jun, Y.-w.; Seo, J.-w.; Cheon, J. *Acc. Chem. Res.* **2008,** 41, (2), 179-189.

[11] Jun, Y.-w.; Lee, J.-H.; Cheon, J. *Angew. Chem. Int. Ed.* **2008,** 47, (28), 5122-5135.

[12] Sun, S.; Zeng, H. *J. Am. Chem. Soc.* **2002,** 124, (28), 8204-8205.

[13] Park, J.; An, K.; Hwang, Y.; Park, J.-G.; Noh, H.-J.; Kim, J.-Y.; Park, J.-H.; Hwang, N.-M.; Hyeon, T. *Nature Mater.* **2004,** 3,

(12), 891-895.

[14] Ho, D.; Sun, X.; Sun, S. *Acc. Chem. Res.* **2011,** 44, (10), 875-882.

[15] Zeng, H.; Black, C. T.; Sandstrom, R. L.; Rice, P. M.; Murray, C. B.; Sun, S. *Phys. Rev. B* **2006,** 73, (2), 020402.

[16] Redl, F. X.; Black, C. T.; Papaefthymiou, G. C.; Sandstrom, R. L.; Yin, M.; Zeng, H.; Murray, C. B.; O'Brien, S. P. *J. Am. Chem. Soc.* **2004,** 126, (44), 14583-14599.

[17] Couchman, P. R.; Jesser, W. A. *Nature* **1977,** 269, (5628), 481-483.

[18] Goldstein, A. N.; Echer, C. M.; Alivisatos, A. P. *Science* **1992,** 256, (5062), 1425-1427.

[19] Jacobs, K.; Zaziski, D.; Scher, E. C.; Herhold, A. B.; Alivisatos, A. P. *Science* **2001,** 293, (5536), 1803-1806.

[20] Chen, C.-C.; Herhold, A. B.; Johnson, C. S.; Alivisatos, A. P. *Science* **1997,** 276, (5311), 398-401.

[21] Lang, X. Y.; Zheng, W. T.; Jiang, Q. *Phys. Rev. B* **2006,** 73, (22), 224444.

[22] Rao, C. N. R.; Kulkarni, G. U.; Thomas, P. J.; Edwards, P. P. *Chem. Eur. J.* **2002,** 8, (1), 28-35.

[23] Polking, M. J.; Han, M.-G.; Yourdkhani, A.; Petkov, V.; Kisielowski, C. F.; Volkov, V. V.; Zhu, Y.; Caruntu, G.; Alivisatos, A. P.; Ramesh, R. *Nature Mater.* **2012,** 11, (8), 700-709.

[24] Banin, U.; Cao, Y.; Katz, D.; Millo, O. *Nature* **1999,** 400, (6744), 542-544.

[25] Lu, A.-H.; Salabas, E. L.; Schüth, F. *Angew. Chem. Int. Ed.* **2007,** 46, (8), 1222-1244.

[26] Zhang, D.; Liu, Z.; Han, S.; Li, C.; Lei, B.; Stewart, M. P.; Tour, J. M.; Zhou, C. *Nano Lett.* **2004,** 4, (11), 2151-2155.

[27] Lee, S.; Fursina, A.; Mayo, J. T.; Yavuz, C. T.; Colvin, V. L.; Sumesh Sofin, R. G.; Shvets, I. V.; Natelson, D. *Nature Mater.* **2008,** 7, (2), 130-133.

[28] Disch, S.; Wetterskog, E.; Hermann, R. l. P.; Salazar-Alvarez, G.; Busch, P.; Bru¨ckel, T.; Bergstro¨m, L.; Kamali, S. *Nano Lett.* **2011,** 11, (4), 1651-1656.

[29] Kim, T. H.; Jang, E. Y.; Lee, N. J.; Choi, D. J.; Lee, K.-J.; Jang, J.-t.; Choi, J.-s.; Moon, S. H.; Cheon, J. *Nano Lett.* **2010,** 10, (7), 2734-2734.

[30] Noh, S.-h.; Na, W.; Jang, J.-t.; Lee, J.-H.; Lee, E. J.; Moon, S. H.; Lim, Y.; Shin, J.-S.; Cheon, J. *Nano Lett.* **2012,** 12, (7), 3716-3721.

[31] Shepherd, J. P.; Koenitzer, J. W.; Aragón, R.; Spal/ek, J.; Honig, J. M. *Phys. Rev. B* **1991,** 43, (10), 8461-8471.

[32] Bednorz, J. G.; Müller, K. A. *Z. Physik B - Condensed Matter* **1986,** 64, (2), 189-193.

[33] Waser, R.; Aono, M. *Nature Mater.* **2007,** 6, (11), 833-840.

[34] Lee, S.; Pirogov, A.; Kang, M.; Jang, K.-H.; Yonemura, M.; Kamiyama, T.; Cheong, S. W.; Gozzo, F.; Shin, N.; Kimura, H.; Noda, Y.; Park, J. G. *Nature* **2008,** 451, (7180), 805-808.

[35] Kim, D.; Lee, N.; Park, M.; Kim, B. H.; An, K.; Hyeon, T. *J. Am. Chem. Soc.* **2009,** 131, (2), 454-455.

[36] Park, J.; Lee, E.; Hwang, N.-M.; Kang, M.; Kim, S. C.; Hwang, Y.; Park, J.-G.; Noh, H.-J.; Kim, J.-Y.; Park, J.-H.; Hyeon, T. *Angew. Chem. Int. Ed.* **2005,** 44, (19), 2872-2877.

[37] Aragón, R.; Buttrey, D. J.; Shepherd, J. P.; Honig, J. M. *Phys. Rev. B* **1985,** 31, (1), 430-436.

[38] Kang, Y.; Ye, X.; Murray, C. B. *Angew. Chem. Int. Ed.* **2010,** 49, (35), 6156-6159.

[39] Lynch, J.; Zhuang, J.; Wang, T.; LaMontagne, D.; Wu, H.; Cao, Y. C. *J. Am. Chem. Soc.* **2011,** 133, (32), 12664-12674.

[40] Rodríguez-Carvajal, J. *Physica B: Condensed Matter* **1993,** 192, (1–2), 55-69.

[41] Thompson, P.; Cox, D. E.; Hastings, J. B. *J. Appl. Crystallogr.* **1987,** 20, (2), 79-83.

[42] Talapin, D. V.; Murray, C. B. *Science* **2005,** 310, (5745), 86-89.

[43] Friedrich, W. *J. Phys.: Condens. Matter* **2002,** 14, (12), R285.

[44] Wright, J. P.; Attfield, J. P.; Radaelli, P. G. *Phys. Rev. B* **2002,** 66, (21), 214422.

[45] Blasco, J.; García, J.; Subías, G. *Phys. Rev. B* **2011,** 83, (10), 104105.

# Chapter 3. Metal–Insulator Transition of $Fe_3O_4$ Nanocrystals by Shell Formation

## 3.1 Introduction

A nanocrystal is a material that has a size of at least one dimension less than 100 nm. Due to this limited size, nanocrystals (NCs) often exhibit different characteristics than bulk [1]. Since pioneer research by M. Faraday in 1857, scientists succeeded to synthesize many different NCs, such as noble metal, semiconductor, metal oxide [2-5]. Since then, scientists have studied how to control size and shape of NCs to improve performance in a variety of applications such as catalyst, energy, and biomedical applications [6-8]. The atoms on the surface of the NCs have chemical bonds that are weak or deficient, as opposed to those located internally. As the size of the NCs decreases, the number of atoms located on the surface and the ratio of the atoms located on the surface increases, so that the physicochemical properties of the NCs change. For example, in the case of melting point, which is considered a material-specific property, NCs have different melting

points than bulk [9-11]. In the case of gold NCs, it is known that the smaller the size, that is, the higher the ratio of the atoms located on the surface, the lower the melting point [12]. This is because the surface atoms has fewer atoms around them, so they have fewer cohesive energy. In addition, there are characteristics that are present in the case of bulk, but become activated with nanoscale. There are many examples of catalysts showing greater activity in nanoscale [13-16]. When atom or molecule, materials have a defined energy level so they show quantum effect. Semiconductor quantum dots show size dependent color and luminescence quality [2, 4, 7, 17-19]. Researchers have found that the heterogenous complex may have another advantage. It also improved the performance of quantum dot by wrapping the shell on the surface of NCs with other materials [18-20]. Sometimes core and shell materials have completely different properties, but they can show new properties by joining them.

Oxide materials are very popular in both academics and industries because of their many fascinating physical properties and numerous important applications. One of the longest known and actively studied materials among the various metal oxide materials is $Fe_3O_4$, also called magnetite. This iron oxide has the Curie temperature

of 858 K. Due to its unique inverse spinel structure, magnetite coexists in a unit cell of $Fe^{2+}$ and $Fe^{3+}$ ions. In 1939, Verwey reported that bulk $Fe_3O_4$, which is fairly conductive with half-metallic character at room temperature, becomes electrically insulating below 123 K, which is now called the Verwey transition temperature ($T_V$) [21]. Above $T_V$, $Fe_3O_4$ has an inverse-spinel structure where half of $Fe^{3+}$ ions occupy tetrahedral sites, and $Fe^{2+}$ and the other half $Fe^{3+}$ are randomly distributed in the octahedral ones. Verwey suggested that this transition is driven by a charge ordering of $Fe^{2+}$ and $Fe^{3+}$ ions in octahedral sites [21]. Recently, it was reported that, below the Verwey transition, $Fe^{2+}$ and $Fe^{3+}$ in octahedral sites form a very unusual three-Fe-site 'trimerons' ground state [22, 23].

Over the last two decades, iron oxide (magnetite ($Fe_3O_4$) and maghemite ($\gamma$-$Fe_2O_3$)) NCs have been intensively investigated for potential applications in biomedicine in various ways, including magnetic resonance imaging (MRI) contrast agents, magnetic biosensors, and heating mediators for magnetic fluid hyperthermia [24-27]. Especially, a recent development in synthetic procedures to produce uniform and size-controllable iron oxide NCs [28, 29] has enabled the size-dependent physical property characterization and their

applications. Despite the tremendous progresses in $Fe_3O_4$ NCs [30-32], however it is still an open question how the metal-insulator transition changes as the other materials are attached.

In this study, we have succeeded in synthesizing uniform-sized $Fe_3O_4$ NCs with precisely controlled metal-ferrite shell. We could synthesize $Fe_3O_4$-Ferrite core-shell NCs by two step seed-mediated growth method. These core-shell of $Fe_3O_4$ NCs sometimes exhibit a clear metal-insulator transition, and sometimes show a repressed metal-insulator transition. Using these well-characterized $Fe_3O_4$ NCs, we could see the impact of metal-ferrite on the metal-insulator transition.

## 3.2 Experimental Section

We synthesized stoichiometric and uniform-sized $Fe_3O_4$ NCs with various ferrite shell using thermal decomposition of iron acetylacetonate ($Fe(acac)_3$) precursor in the presence of oleic acid surfactant. We could synthesize core-shell NCs by two step method.

Materials.

Iron(III) acetylacetonate (99+%) was purchased from Acros organics. Manganese(II) acetylacetonate, $CoCl_2$, Nickel(II) acetylacetonate, $CuCl_2$, Zinc (II)acetylacetonate hydrate were purchased from Sigma-Aldrich (Merck). Oleic acid (technical grade, 90%) and benzyl ether (98%) were purchased from Sigma-Aldrich (Merck). These chemicals are used without further purification.

Synthesis of $Fe_3O_4$ core nanocrystals

The procedure for the synthesis of 26nm sized $Fe_3O_4$ NCs is as follows. 21.3g (60mmol) iron(III) acetylacetonate and 33.9g (120mmol) oleic acid were dissolved in 312.0g (300ml) benzyl ether. The mixture

was degassed for 1hr at room temperature by using rotary vacuum pump. Very fast stirring is essential throughout the synthesis process to synthesize uniform NCs. The mixture was heated up to 290 ℃ under $CO/CO_2$ 4/96 (in mass ratio) gas. Carbon monoxide (CO) gas is used as a reducing agent to control oxygen stoichiometry of $Fe_3O_4$ NCs [33]. Boil the solution at 290 ℃ for 30 minutes, then remove the heating mantle and cool it down. After cooling to room temperature, centrifuge the mixture at 8000 rpm for 10 minutes to precipitate $Fe_3O_4$ NCs. The precipitate was washed several times more using toluene and ethanol as solvent and nonsolvent. As-synthesized NCs were stored in inert gas to avoid oxidation after synthesis.

With the 5 nm-sized NCs as seeds, larger NCs up to 14 nm can be synthesized by seed-mediated growth method (Figure 3.1). After the synthesis of 5 nm NCs, more precursor, surfactant and solvent are injected into the crude product. For example, when 1.13 g of iron(III) acetylacetonate, 3.39 g of oleic acid, 31.2 g of benzyl ether were injected into the crude 5 nm-sized NCs product and heated up, 6 nm-sized NCs were produced. We could get $Fe_3O_4$ NCs with diameters of 8, 10, 14 nm by repeating the above seed-mediated growth process.

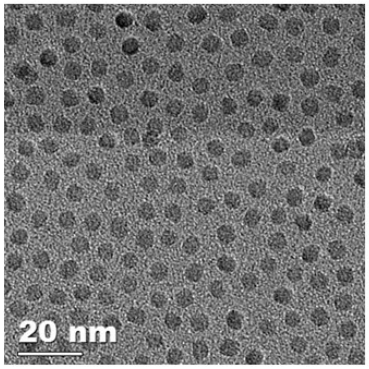
20 nm

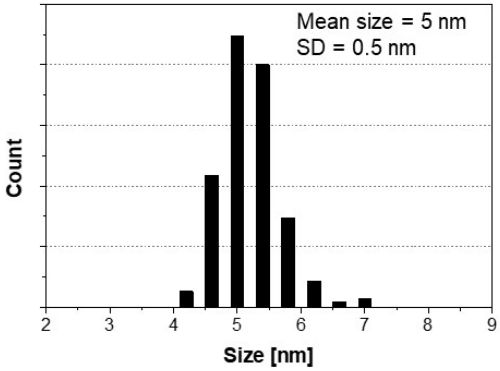
Mean size = 5 nm
SD = 0.5 nm
Count
2
3
4
5
6
7
8
9
Size [nm]

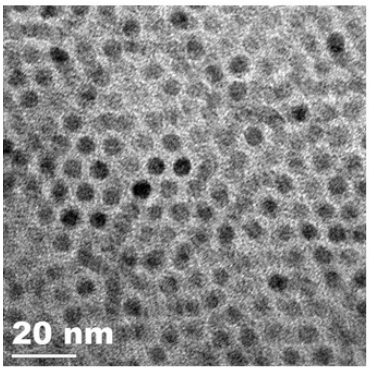
20 nm

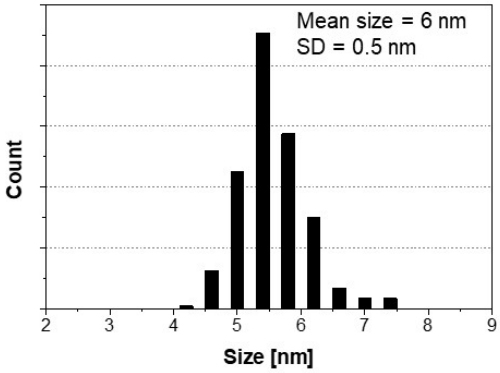
Mean size = 6 nm
SD = 0.5 nm
Count
2
3
4
5
6
7
8
9
Size [nm]

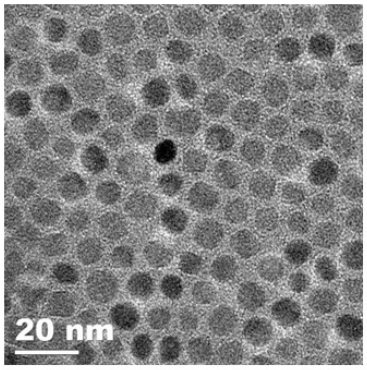
20 nm

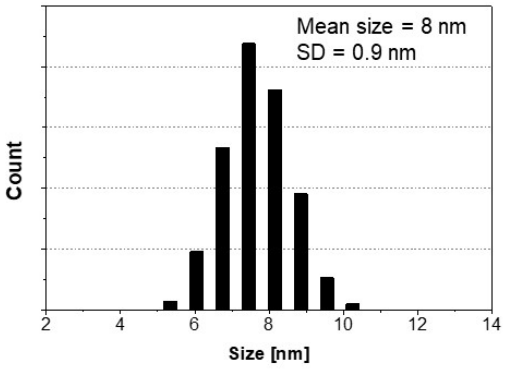
Mean size = 8 nm
SD = 0.9 nm
Count
2
4
6
8
10
12
14
Size [nm]

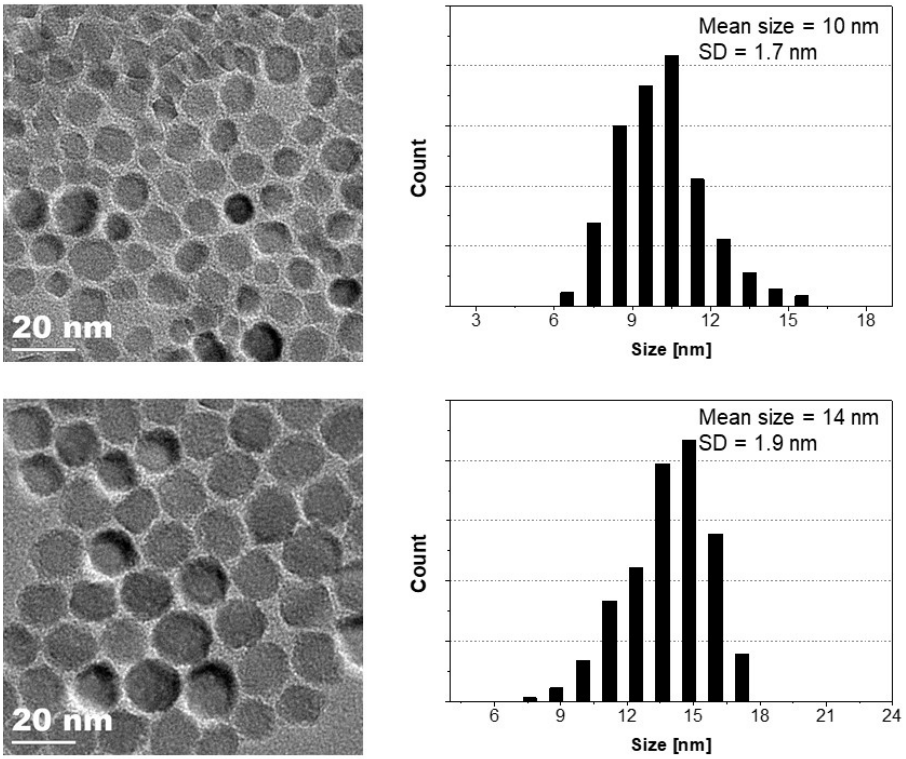


**Figure 3.1** TEM images and size distribution histograms of seed-mediated grown $Fe_3O_4$ NCs.

Synthesis of $Fe_3O_4$ core with metal-ferrite shell NCs

Put the manganese(II) acetylacetonate 0.5 mmol, iron(III) acetylacetonate 1.0 mmol, the oleic acid 8 mmol, and the benzyl ether 20 ml (20.8 g) into the round-bottom flask. Mix the mixture as quickly as possible with a magnetic stirrer, and use the rotary pump to degas it at room temperature for one hour. Change the round-bottom flask containing this mixture to the Ar gas state and then inject 3ml of the crude oil of $Fe_3O_4$ NCs. Increase the mixture with $Fe_3O_4$ NCs to 290 ℃ and maintain for 30 minutes. Then, remove the heating mantle and cool it to room temperature. Pour some toluene and a large amount of ethanol into $Fe_3O_4$-$MnFe_2O_4$ core-shell NCs crude oil. And with centrifuge, the $Fe_3O_4$-$MnFe_2O_4$ core-shell NCs sink. Repeat this washing process 3 times to remove as much organic matter as possible. Vacuum dry, dusted, and later used for analysis. In order to make other metal-ferrite shell, only the manganese(II) acetylacetonate can be replaced with another precursor in the above process. You can use the iron(III) acetylacetonate to make $Fe_3O_4$ shell and Cobalt(II) acetylacetonate to make $CoFe_2O_4$ shell. You can use Nickel(II) acetylacetonate to make $NiFe_2O_4$ shell, or Copper(II) acetylacetonate to make $CuFe_2O_4$ shell. To synthesize $ZnFe_2O_4$ shell, use Zinc(II) chloride.

Characterization

We stored and characterized the NCs in either inert atmosphere or high vacuum throughout the experiments so that the chance for oxidation after synthesis was minimal. In all measurements, the time to expose samples to air was minimized to reduce oxidation problems.

TEM measurement.

JEOL JEM-2100F electron microscope with 200 kV was used for TEM images and EDS measurement. Before making a TEM sample grid, remove the organics through sufficient washing process. Sample grid was prepared by sonicating the NCs dispersion in toluene and dropping onto ultrathin carbon film coated copper grid. Remove any remaining organic substances by heat treatment of the TEM sample grid at 450 ℃ for 30 seconds just before the EDS measurement.

X-ray diffraction.

The powder X-ray diffraction (XRD) patterns were obtained with a Rigaku D/Max 2500 diffractometer equipped with a rotating

anode and a Cu radiation source ($\lambda$ = 0.15418 nm). Place the NCs on top of the silica substrate to measure XRD.

Magnetic moment measurement.

Magnetization measurements were performed using a Quantum Design SQUID magnetometer MPMS 5XL. Insert the powder NCs into the gelatin capsule for MPMS measurement. Insert this gelatin capsule into the plastic straw and make a MPMS measurement.

## 3.3 $Fe_3O_4$-$Fe_3O_4$ core-shell nanocrystals

First, we employed seed-mediated growth process to synthesize $Fe_3O_4$ NCs with sizes of 5～14 nm (Figure 3.1) [34]. In seed-mediated growth experiments, we used 5 nm NCs as the seeds to prepare 6, 8, 10, and 14 nm NCs (Figure 3.2A) [34, 35]. In this way, we obtained the larger NCs with their core having the stoichiometry of the smaller seed NCs. If the size of the NCs affects the $Fe^{3+}/Fe^{2+}$ ratio, then the metal-insulator transition behaviors of the NCs prepared by seed-mediated growth method and by the one-pot synthesis method (heating $Fe(acac)_3$ solution without the seeds) should be different [36]. If the metal-insulator transition of the $Fe_3O_4$ core disappears due to $Fe_3O_4$ shell formation, it may be thought there is a problem with the synthetic process. As shown in Figure 3.2B, zero-field-cooled (ZFC) magnetization data reveal that there are clear stepwise magnetic moment changes near 120 K in the 10 and 14 nm samples, which coincide almost perfectly with the data from the NCs with the same sizes but prepared by the one-pot thermal-decomposition method [36]. This observation confirms that the size of the NCs has nearly no effect on the stoichiometry of $Fe_3O_4$ NCs and the size-dependent behavior of the metal-insulator transition is reproducible with good reliability from

the samples prepared via two different synthetic methods. And of course, we can see that $Fe_3O_4$ shell does not adversely affect the metal-insulator transition of the existing $Fe_3O_4$ core. Rather, It behaves as if the size of $Fe_3O_4$ core increased by the thickness of the shell, indicating that the temperature of the metal-insulator transition rises slightly as previously studied [36].

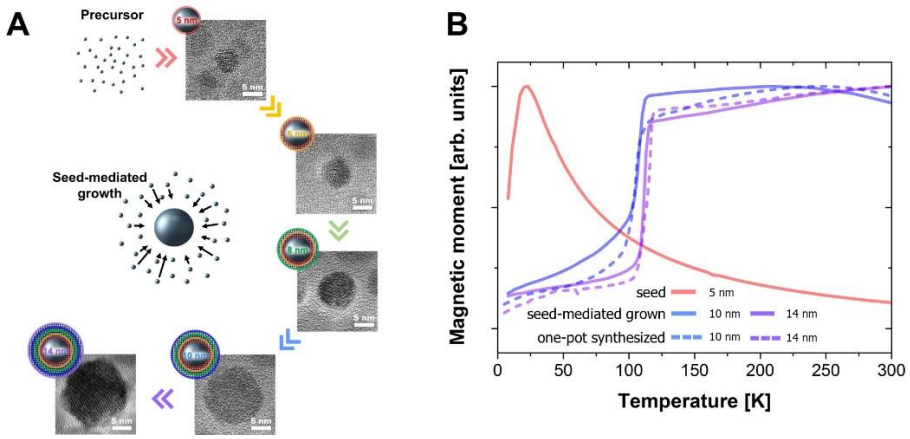


**Figure 3.2** Evolution of the metal-insulator transition in $Fe_3O_4$ NCs with sizes from 5 to 14 nm. (A) $Fe_3O_4$ NCs with sizes of 6, 8, 10, and 14 nm were synthesized using 5 nm-sized NCs as seeds. (B) Zero-field-cooled (ZFC) magnetization data is measured under field of 10 mT. The stepwise magnetic moment change near 120 K indicates the metal-insulator transition. Note that the $T_V$ of seed-mediated grown NCs (solid line) and one-pot synthesized NCs (dotted line) are nearly identical.

## 3.4 $Fe_3O_4$-$MFe_2O_4$ (M= Mn, Co, Ni, CU, Zn) core-shell nanocrystals

Thus, the $Fe_3O_4$ shell did not cause any unusual changes in the metal-insulator transition. Now, the question arises as to what will happen if the $Fe_3O_4$ core is wrapped with a material other than $Fe_3O_4$. So, we decided to wrap the $Fe_3O_4$ core NC with a shell other than $Fe_3O_4$. However, there are several conditions to wrap the shell with something other than $Fe_3O_4$. In the wrapping shell process, a nucleus formed at the surface of a core can be stabilized by the interface with the core, which radically changes the energetics of the nucleation reaction compared with that of homogeneous nucleation. In general, the interface energy is the main factor that determines the shape of the nucleus in heterogeneous nucleation, as well as the height of the energy barrier of the nucleation reaction. Correspondingly, in heterogeneous nucleation, there is a strong tendency to minimize the interface energy of the nucleus and the seed. If the nucleus and the seed form a heteroepitaxial interface, the interface energy increases with their lattice mismatch. As a result, their lattices are mechanically strained to

reduce the mismatch at the interface. Therefore, materials with the same crystal structure as $Fe_3O_4$ and not much difference in the lattice parameters can be considered optimal materials as a shell of $Fe_3O_4$ NCs.

Ferrite is a ferrimagnetic ceramic material that shows hard, brittle, and poor electrical conductivity. Many Ferrite materials have a spinnel structure called $AB_2O_4$. Among them, A and B represent several metal cations and if A and B are all Fe, it becomes magnetite ($Fe_3O_4$). Other than $Fe_3O_4$, there are $MnFe_2O_4$, $CoFe_2O_4$, $NiFe_2O_4$, $CuFe_2O_4$, and $ZnFe_2O_4$. All of these ferrite materials have the same cubic close-packed (FCC) structure, and the difference in lattice parameter values is not significant (Table 3.1). Because these ferrite materials have the same crystal structure as $Fe_3O_4$, the XRD pattern is also located in the same location.

| Ferrite composition | Crystal system | Space group | Lattice parameter (Å) | Volume of cell ($\times 10^6$ pm$^3$) |
|---|---|---|---|---|
| $MnFe_2O_4$ | Cubic | $Fd\bar{3}m$ | 8.4970 | 613.47 |
| $Fe_3O_4$ | | | 8.3960 | 591.86 |
| $CoFe_2O_4$ | | | 8.3900 | 590.59 |
| $NiFe_2O_4$ | | | 8.3390 | 579.89 |
| $CuFe_2O_4$ | | | 8.3730 | 587.01 |
| $ZnFe_2O_4$ | | | 8.4270 | 598.44 |

**Table 3.1** Crystal structure and lattice parameter of various ferrite materials. It can be seen that all ferrite materials have the same crystal structure as $Fe_3O_4$. Also, compared to $Fe_3O_4$, the difference in lattice parameter values is only about 1% [37-42]. XRD peak can be found to be the same as the crystal structure.

The same $Fe_3O_4$ core NCs were used in all of the synthetic processes to clearly see the impact on the metal-insulator transition of the ferrite shell. $Fe_3O_4$ NCs, which play the core during seed-mediated growth, have a size of about 26 nm (Figure 3.3A). Core $Fe_3O_4$ NCs were synthesized in the same way as was shown in the previous reference [36]. And when we take a magnetic measurement (ZFC, Zero Field Cooling at 10 mT) of core $Fe_3O_4$ NCs, we can see that there is a distinct variation in the magnetic moment of stairs near 120 K. This change is proof of the metal-insulator transition (Figure 3.3B). Core $Fe_3O_4$ NCs are confirmed to be synthesized in stoichiometry ratio 3:4. The reasons for using 26 nm sized $Fe_3O_4$ core NCs are as follows. First, the smaller $Fe_3O_4$ NCs shows the metal-insulator transition at temperatures below 120 K [36]. When the metal-insulator transition temperature changes in the hetero structure, it is not clear whether the core NCs' size affects or whether the hetero structure affects. Second, the separation line is not clearly defined when the hetero structure is formed, and a certain portion of a boundary line forms an alloy. This alloy part will be only several nm thick at the most, so by using 26 nm $Fe_3O_4$ core NCs, we could exclude the effects of alloy formation. XRD was measured to confirm composition of core-shell NCs synthesized by

seed-mediated growth method. According to the XRD pattern, no peak other than the $Fe_3O_4$ Bragg peak (red line) was detected (Figure 3.4). The synthesized core-shell NCs are composed of $Fe_3O_4$ and $MFe_2O_4$ (M= Mn, Co, Ni, Cu, Zn) in terms of having the same Bragg peak as $Fe_3O_4$ (Figure 3.5). In other words, it can be confirmed that there are no impurities such as CoO or MnO.

A magnetic moment measurement was made to determine the effect of the ferrite shell on the metal-insulator transition of $Fe_3O_4$ core NCs (Figure 3.6). Put the synthesized core-shell NCs into the gelatin capsule and measure ZFC (Zero field cooling) at 10 mT. It shows almost the same magnetic behavior of $Fe_3O_4$-$MnFe_2O_4$ core-shell, $Fe_3O_4$-$NiFe_2O_4$ core-shell, $Fe_3O_4$-$CuFe_2O_4$ core-shell, $Fe_3O_4$-$ZnFe_2O_4$ core-shell NCs with that of $Fe_3O_4$ core NCs. Therefore, we can see that this shell material does not affect the metal-insulator transition of $Fe_3O_4$ NCs. On the other hand, core-shell NCs formed by $CoFe_2O_4$ shell show that unlike $Fe_3O_4$ core NCs, there is no significant variation in the magnetic moment at 120 K. Meanwhile, $Fe_3O_4$ with the Co atom doped is known to undergo metal-insulator transition at temperatures below 120 K [43]. However, if we look at ZFC data when $CoFe_2O_4$ shell is present, no step-wise changes are observed around 120 K. In other

words, the presence of $CoFe_2O_4$ shell inhibits the metal-insulator transition of $Fe_3O_4$ NCs. We don't know exactly why this happens yet, but we can make the following guess. $CoFe_2O_4$ belongs to the ferrite family, but it is the only hard ferrite material among $MnFe_2O_4$, $Fe_3O_4$, $NiFe_2O_4$, $CuFe_2O_4$, $ZnFe_2O_4$. Hard ferrite material means that the crystal anisotropy is high. A crystal anisotropy is a force which tends to align the magnetization in a particular crystallographic direction. Therefore, we can guess that the high crystal anisotropy of $CoFe_2O_4$ is affecting the metal-insulator transition of $Fe_3O_4$ NCs.

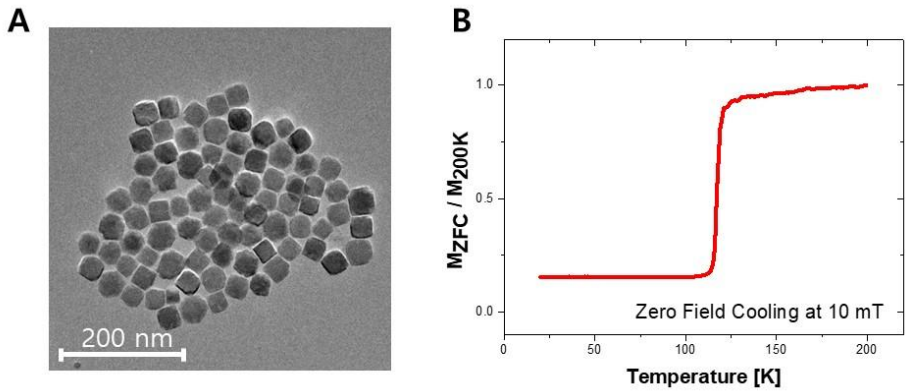


**Figure 3.3** TEM image of $Fe_3O_4$ NCs used as core during the seed-mediated growth process. Core NCs have a uniform size (A). ZFC (Zero field cooling) magnetization data of Core $Fe_3O_4$ NCs. The magnetization value varies greatly in the vicinity of the 120 K, just like the shape of a stair. The change in the magnetization of these stair shapes is a clear indication of the metal-insulator transition of $Fe_3O_4$ NCs (B).

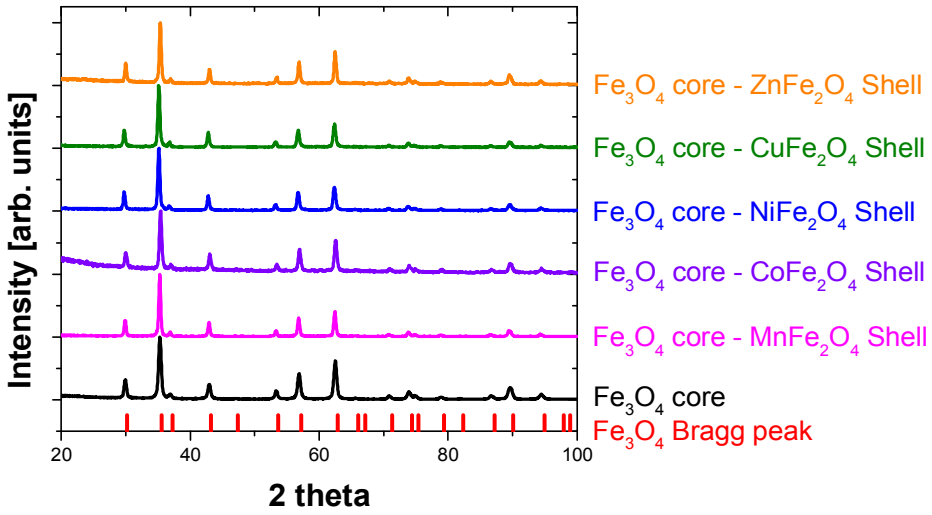


**Figure 3.4** X-ray diffraction pattern of synthesized $Fe_3O_4$ NCs and $Fe_3O_4$-Ferrite core-shell NCs. All NCs show XRD peak like $Fe_3O_4$ Bragg peak. Given that the XRD peak position of the ferrite materials is the same as $Fe_3O_4$, it is shown that no other impurities were produced except ferrite and $Fe_3O_4$.

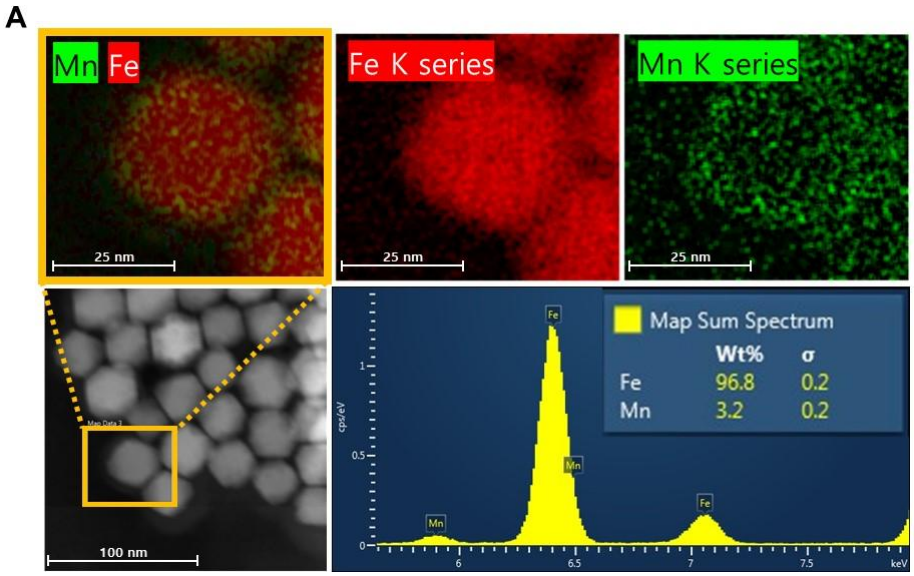
A
Mn Fe
25 nm
Fe K series
25 nm
Mn K series
25 nm
100 nm
Map Sum Spectrum
Wt% σ
Fe 96.8 0.2
Mn 3.2 0.2
cps/eV
keV

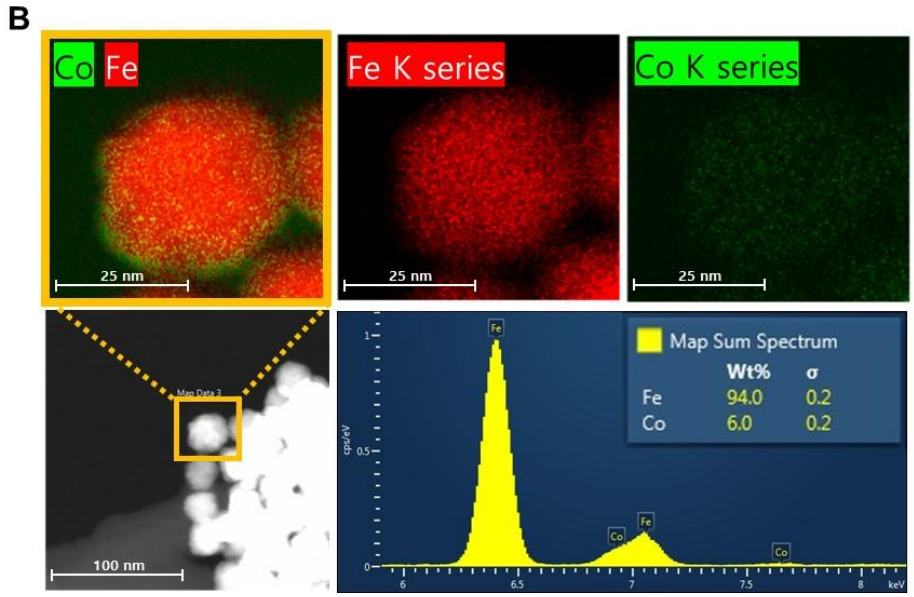
B
Co Fe
25 nm
Fe K series
25 nm
Co K series
25 nm
100 nm
Map Sum Spectrum
Wt% σ
Fe 94.0 0.2
Co 6.0 0.2
cps/eV
keV

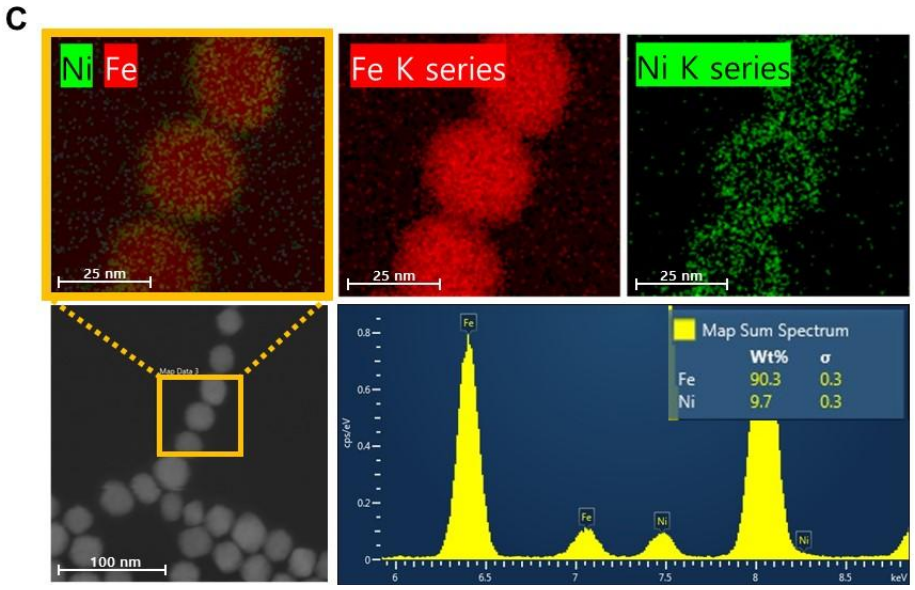
C
Ni Fe
25 nm
Fe K series
25 nm
Ni K series
25 nm
100 nm
Map Sum Spectrum
Wt% σ
Fe 90.3 0.3
Ni 9.7 0.3
cps/eV
keV

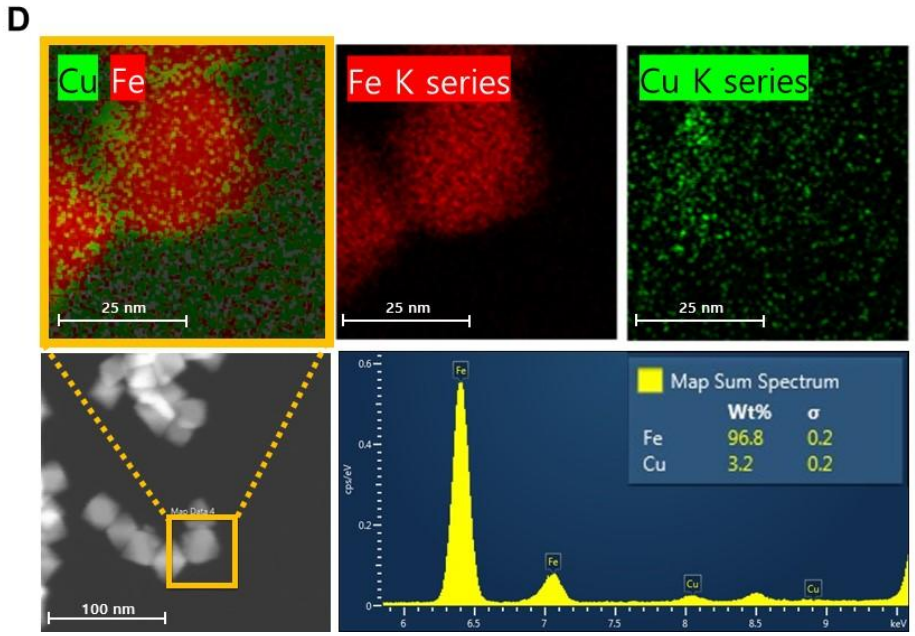
D
Cu Fe
25 nm
Fe K series
25 nm
Cu K series
25 nm
100 nm
Map Sum Spectrum
Wt% σ
Fe 96.8 0.2
Cu 3.2 0.2
cps/eV
keV

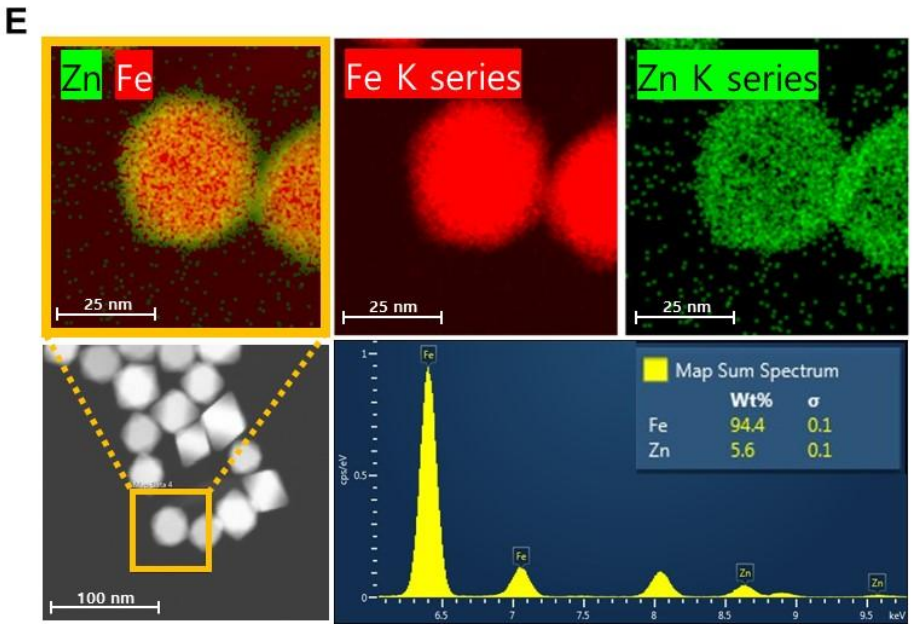


**Figure 3.5** Core-shell NCs synthesized by seed-mediated growth method. We know that (A) was created by $MnFe_2O_4$, (B) by $CoFe_2O_4$, (C) by $NiFe_2O_4$, (D) by $CuFe_2O_4$, and (E) by $ZnFe_2O_4$ shell. In the lower left corner of each figure, there is a STEM image taken at a low magnification. The results of EDS mapping by selecting one of the NCs are at the top of each figure. You can see the distribution of each metal atoms. The distribution of Mn, Co, Ni, Cu and Zn atoms to the surface of NCs indicates a core-shell structure. In the lower right corner of each figure, the quantitative analysis of the metallic atoms can be checked.

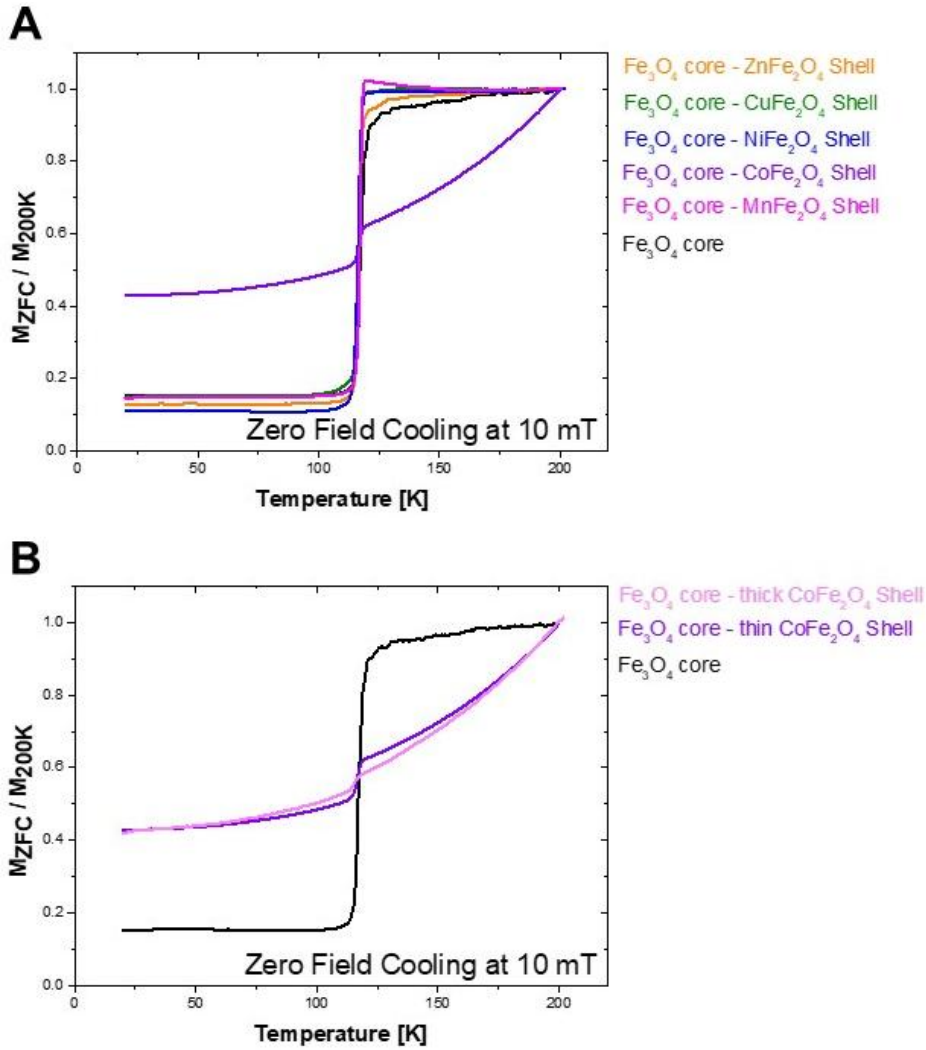


**Figure 3.6** The ZFC magnetic moment data of core-shell NCs which are synthesized by seed-mediated growth method. Core-shell NCs with $MnFe_2O_4$, $NiFe_2O_4$, $CuFe_2O_4$, $ZnFe_2O_4$ shell exhibit the same step-wise magnetic moment changes near 120 K as $Fe_3O_4$ core NCs. On the other hand, core-shell NCs with $CoFe_2O_4$ shell have greatly reduced the step-wise variation in the magnetic moment (A). By

making the $CoFe_2O_4$ shell thicker, you can see that the variation in the step-wise value is reduced. In other words, we see that the presence of $CoFe_2O_4$ shell has an impact on the metal-insulator transition (B).

## 3.5 Conclusions

In summary, the core-shell structure was synthesized to see the change in the metal-insulator transition of $Fe_3O_4$ NCs. Shell materials used were $MnFe_2O_4$, $Fe_3O_4$, $CoFe_2O_4$, $NiFe_2O_4$, $CuFe_2O_4$, and $ZnFe_2O_4$. Although we could not observe any unusual changes in other materials, we could confirm that the metal-insulator transition was extinguished if there was $CoFe_2O_4$ shell. More research will be needed to determine the cause.

## 3.6 References


[1] Faraday, M. *Philosophical Transactions of the Royal Society of London* **1857,** 147, 145-181.

[2] Murray, C. B.; Norris, D. J.; Bawendi, M. G. *J. Am. Chem. Soc.* **1993,** 115, (19), 8706-8715.

[3] Wang, X.; Zhuang, J.; Peng, Q.; Li, Y. *Nature* **2005,** 437, (7055), 121-124.

[4] Alivisatos, A. P. *Science* **1996,** 271, (5251), 933-937.

[5] Park, J.; An, K.; Hwang, Y.; Park, J.-G.; Noh, H.-J.; Kim, J.-Y.; Park, J.-H.; Hwang, N.-M.; Hyeon, T. *Nature Mater.* **2004,** 3, (12), 891-895.

[6] Sun, Y.; Xia, Y. *Science* **2002,** 298, (5601), 2176-2179.

[7] Peng, X.; Manna, L.; Yang, W.; Wickham, J.; Scher, E.; Kadavanich, A.; Alivisatos, A. P. *Nature* **2000,** 404, (6773), 59-61.

[8] Chen, C.; Kang, Y.; Huo, Z.; Zhu, Z.; Huang, W.; Xin, H. L.;

Snyder, J. D.; Li, D.; Herron, J. A.; Mavrikakis, M.; Chi, M.; More, K. L.; Li, Y.; Markovic, N. M.; Somorjai, G. A.; Yang, P.; Stamenkovic, V. R. *Science* **2014,** 343, (6177), 1339-1343.

[9] Goldstein, A. N.; Echer, C. M.; Alivisatos, A. P. *Science* **1992,** 256, (5062), 1425-1427.

[10] Lai, S. L.; Guo, J. Y.; Petrova, V.; Ramanath, G.; Allen, L. H. *Phys. Rev. Lett.* **1996,** 77, (1), 99-102.

[11] Jiang, Q.; Tong, H. Y.; Hsu, D. T.; Okuyama, K.; Shi, F. G. *Thin Solid Films* **1998,** 312, (1–2), 357-361.

[12] Buffat, P.; Borel, J. P. *Physical Review A* **1976,** 13, (6), 2287.

[13] Jones, J.; Xiong, H.; DeLaRiva, A. T.; Peterson, E. J.; Pham, H.; Challa, S. R.; Qi, G.; Oh, S.; Wiebenga, M. H.; Pereira Hernández, X. I.; Wang, Y.; Datye, A. K. *Science* **2016,** 353, (6295), 150.

[14] Huang, X.; Zhao, Z.; Cao, L.; Chen, Y.; Zhu, E.; Lin, Z.; Li, M.; Yan, A.; Zettl, A.; Wang, Y. M.; Duan, X.; Mueller, T.; Huang, Y. *Science* **2015,** 348, (6240), 1230-1234.

[15] Hernandez-Fernandez, P.; Masini, F.; McCarthy, D. N.; Strebel, C. E.; Friebel, D.; Deiana, D.; Malacrida, P.; Nierhoff, A.; Bodin, A.; Wise, A. M.; Nielsen, J. H.; Hansen, T. W.; Nilsson, A.; StephensIfan, E. L.; Chorkendorff, I. *Nat Chem* **2014,** 6, (8), 732-738.

[16] Wang, D.; Li, Y. *Adv. Mater.* **2011,** 23, (9), 1044-1060.

[17] Alivisatos, A. P. *The Journal of Physical Chemistry* **1996,** 100, (31), 13226-13239.

[18] Dabbousi, B. O.; Rodriguez-Viejo, J.; Mikulec, F. V.; Heine, J. R.; Mattoussi, H.; Ober, R.; Jensen, K. F.; Bawendi, M. G. *J. Phys. Chem. B* **1997,** 101, (46), 9463-9475.

[19] Peng, X.; Schlamp, M. C.; Kadavanich, A. V.; Alivisatos, A. P. *J. Am. Chem. Soc.* **1997,** 119, (30), 7019-7029.

[20] Cao; Banin, U. *J. Am. Chem. Soc.* **2000,** 122, (40), 9692-9702.

[21] Verwey, E. J. *Nature* **1939,** 144, (3642), 327-328.

[22] Senn, M. S.; Wright, J. P.; Attfield, J. P. *Nature* **2012,** 481,

(7380), 173-176.

[23] Senn, M. S.; Loa, I.; Wright, J. P.; Attfield, J. P. *Phys. Rev. B* **2012,** 85, (12), 125119.

[24] Laurent, S.; Forge, D.; Port, M.; Roch, A.; Robic, C.; Vander Elst, L.; Muller, R. N. *Chem. Rev.* **2008,** 108, (6), 2064-2110.

[25] Stanley, S. A.; Gagner, J. E.; Damanpour, S.; Yoshida, M.; Dordick, J. S.; Friedman, J. M. *Science* **2012,** 336, (6081), 604-608.

[26] Cheng, K.; Peng, S.; Xu, C.; Sun, S. *J. Am. Chem. Soc.* **2009,** 131, (30), 10637-10644.

[27] Xie, J.; Liu, G.; Eden, H. S.; Ai, H.; Chen, X. *Acc. Chem. Res.* **2011,** 44, (10), 883-892.

[28] Sun, S.; Zeng, H. *J. Am. Chem. Soc.* **2002,** 124, (28), 8204-8205.

[29] Kim, D.; Lee, N.; Park, M.; Kim, B. H.; An, K.; Hyeon, T. *J. Am. Chem. Soc.* **2009,** 131, (2), 454-455.

[30] Chen, J.; Ye, X.; Oh, S. J.; Kikkawa, J. M.; Kagan, C. R.; Murray, C. B. *ACS Nano* **2012,** 7, (2), 1478-1486.

[31] Zeng, H.; Li, J.; Liu, J. P.; Wang, Z. L.; Sun, S. *Nature* **2002,** 420, (6914), 395-398.

[32] Chen, J.; Dong, A.; Cai, J.; Ye, X.; Kang, Y.; Kikkawa, J. M.; Murray, C. B. *Nano Lett.* **2010,** 10, (12), 5103-5108.

[33] Aragón, R.; Buttrey, D. J.; Shepherd, J. P.; Honig, J. M. *Phys. Rev. B* **1985,** 31, (1), 430-436.

[34] Park, J.; Lee, E.; Hwang, N.-M.; Kang, M.; Kim, S. C.; Hwang, Y.; Park, J.-G.; Noh, H.-J.; Kim, J.-Y.; Park, J.-H.; Hyeon, T. *Angew. Chem. Int. Ed.* **2005,** 44, (19), 2872-2877.

[35] Sun, S.; Zeng, H.; Robinson, D. B.; Raoux, S.; Rice, P. M.; Wang, S. X.; Li, G. *J. Am. Chem. Soc.* **2004,** 126, (1), 273-279.

[36] Lee, J.; Kwon, S. G.; Park, J.-G.; Hyeon, T. *Nano Lett.* **2015,** 15, (7), 4337-4342.

[37] Denecke, M. A.; Gunßer, W.; Buxbaum, G.; Kuske, P. *Mater.*

*Res. Bull.* **1992,** 27, (4), 507-514.

[38] Wechsler, B. A.; Lindsley, D. H.; Prewitt, C. T. *Am. Mineral.* **1984,** 69, (7-8), 754-770.

[39] Lefevre, C.; Roulland, F.; Viart, N.; Greneche, J. M.; Pourroy, G. *J. Solid State Chem.* **2010,** 183, (11), 2623-2630.

[40] Sawaoka, A.; Kawai, N. *J. Phys. Soc. Jpn.* **1968,** 25, (1), 133-140.

[41] Gomes, J. A.; Sousa, M. H.; Tourinho, F. A.; Mestnik-Filho, J.; Itri, R.; Depeyrot, J. *J. Magn. Magn. Mater.* **2005,** 289, 184-187.

[42] Slatineanu, T.; Iordan, A. R.; Palamaru, M. N.; Caltun, O. F.; Gafton, V.; Leontie, L. *Mater. Res. Bull.* **2011,** 46, (9), 1455-1460.

[43] Brabers, V. A. M.; Walz, F.; Kronmüller, H. *Phys. Rev. B* **1998,** 58, (21), 14163-14166.

# Bibliography

## Journal Publication


1. **Lee, J.**; Kwon, S. G.; Park, J.-G.; Hyeon, T.

   Size Dependence of Metal–Insulator Transition in Stoichiometric $Fe_3O_4$ Nanocrystals.

   *Nano Lett.* **2015**, 15, (7), 4337-4342.

2. **Lee, J.**; Yang, J.; Kwon, S. G.; Hyeon, T.

   Nonclassical nucleation and growth of inorganic nanoparticles.

   *Nature Reviews Materials* **2016**, 1, 16034.

3. Oh, M. H.; Lee, N.; Kim, H.; Park, S. P.; Piao, Y.; **Lee, J.**; Jun, S. W.; Moon, W. K.; Choi, S. H.; Hyeon, T.

   Large-Scale Synthesis of Bioinert Tantalum Oxide Nanoparticles for X-ray Computed Tomography Imaging and Bimodal Image-Guided Sentinel Lymph Node Mapping.

   *J. Am. Chem. Soc.* **2011**, 133, (14), 5508-5515.

4. Kim, B. H.; Shin, K.; Kwon, S. G.; Jang, Y.; Lee, H.-S.; Lee, H.; Jun, S. W.; **Lee, J.**; Han, S. Y.; Yim, Y.-H.; Kim, D.-H.; Hyeon, T.

Sizing by Weighing: Characterizing Sizes of Ultrasmall-Sized Iron Oxide Nanocrystals Using MALDI-TOF Mass Spectrometry.

*J. Am. Chem. Soc.* **2013**, 135, (7), 2407-2410.

5. Lee, D. J.; Yu, S.-H.; Lee, H. S.; Jin, A.; **Lee, J.**; Lee, J. E.; Sung, Y.-E.; Hyeon, T.

Facile synthesis of metal hydroxide nanoplates and their applications to lithium ion battery anodes.

*Journal of Materials Chemistry A* **2017**, 5, (18), 8744-8751.

6. Lim, S.; Choi, B.; Lee, S. Y.; Lee, S.; Nahm, H.-H.; Kim, Y.-H.; Kim, T.; Park, J.-G.; **Lee, J.**; Hong, J.; Kwon, S. G.; Hyeon, T.

Microscopic States and the Verwey Transition of Magnetite Nanocrystals Investigated by Nuclear Magnetic Resonance.

*Nano Lett.* **2018**, 18, (3), 1745-1750.

7. Kwon, H. J.; Shin, K.; Soh, M.; Chang, H.; Kim, J.; **Lee, J.**; Ko, G.; Kim, B. H.; Kim, D.; Hyeon, T.

Large-Scale Synthesis and Medical Applications of Uniform-Sized Metal Oxide Nanoparticles.

*Adv. Mater.* **2018**, 30, (42), 1704290.

# 초 록

나노입자는 적어도 한쪽 방향의 너비가 100 nm, 다시 말해 천만 분의 1미터 이하의 크기를 가진 입자이다. 나노입자는 기존의 벌크 물질과는 달리, 하나의 입자를 구성하는 원자의 개수가 매우 적다. 이로 인해서 기존 벌크 물질과는 다른 물리적, 화학적 성질을 지닐 수 있다. 지난 수십 년에 걸쳐서 이러한 차이를 확인하는 연구 및 공학적으로 이용하려는 연구가 많이 진행되고 있다.

한편, 원하는 성질의 나노입자를 실질적으로 활용하기 위해서는 나노입자를 균일하면서도 원하는 모양으로 만들 수 있어야 한다. 본 논문의 첫 번째 장에서는 어떻게 나노입자를 합성해야 균일하면서도 원하는 모양으로 만들 수 있는지 알아보았다. 이렇게 합성된 다양한 종류 및 크기의 나노입자를 가지고 나노입자만이 가지는 특이한 성질을 연구할 수 있었다. 두 번째 장에서는 다양한 크기로 합성된 산화철 나노입자를 가지고 금속-절연체 전이 현상을 관찰하였다. 나노입자의

크기가 작아질수록 금속-절연체 전이 현상에 큰 변화가 생기는 것을 알 수 있었다. 세 번째 장에서는 산화철 나노입자에 껍질구조를 만들어서 금속-절연체 전이 현상의 변화를 관찰하였다. 껍질이 되는 물질의 종류 및 껍질의 두께가 달라짐에 따라서 금속-절연체 전이 현상에도 변화가 생기는 것을 알 수 있었다.

**주요어:** 나노입자, 산화철, 금속-절연체 전이현상

**학 번:** 2010-22819